Ion Temperature and Flow Velocity Measurements on SSX-FRC

Aongus Ó Murchadha

Senior Honors Thesis

Swarthmore College Department of Physics and Astronomy
500 College Avenue, Swarthmore, PA 19081

March 15, 2005

Abstract

An Ion Doppler Spectroscopy (IDS) diagnostic was used to measure the flow velocity and temperature of a plasma created by SSX-FRC. The diagnostic was based on the principles of Doppler spectroscopy, namely, that the wavelength of a moving light source is shifted proportional to its velocity and the width of an emission line varies with temperature. The emission line at 229.7 nm of Carbon III, an impurity ion in the hydrogen plasma, was imaged and its location and width measured. The IDS system being a work in progress, the minimum resolvable linewidth is higher than the linewidth we expect to see based on previous experiments and so detailed temperature and velocity measurements could not be carried out. SSX's PMT's allow detailed time resolution and the plot of temperature variation with time shows that the width of the line peaks between 30 and 50 μs before it drops to the minimum resolvable width. Considering the basic plasma physics of the system, it is thought that the wide line is due to velocity shear: oppositely directed jets resulting from magnetic reconnection create both a red- and a blue-shifted emission line, which overlap and are imaged as a single, very wide, line. A simple analytical model of a fluid system with velocity shear was created to investigate whether or not shear could cause the widening. The lineshapes this model returned were wide and double-peaked due to overlap, supporting the shear hypothesis.

Contents

1 Introduction

Comprising perhaps 95% of the visible universe, plasmas are gases existing under conditions that cause atoms to ionize. These conditions are generally high temperature combined with a low recombination rate, often due to a low number density of particles. The result is a diffuse, gaseous mixture of ions and electrons. Although superficially similar, gases and plasmas behave quite differently, primarily in their responses to electromagnetic fields. The constituent particles of ideal gases interact over length scales on the order of an atomic diameter, but plasma particles attract and repel one another via Coulombic interactions, over length scales significantly greater than those in ideal gases. As a collection of free charged particles, plasmas are good conductors and so permit currents to flow through them. Moreover, plasmas respond dynamically to the fields generated by these currents, resulting in behavior of incredible complexity. Due to their low density, plasmas allow some electrostatic and electromagnetic waves to propagate, unlike solid conductors that attenuate most incident fields [16].

Our ability to study and control plasmas is hampered by our inhospitable environment. Plasmas exposed to Earth-like temperatures quickly lose their energy through diffusion to the cooler surroundings, and the constituent ions and electrons can no longer move quickly enough to avoid recombining as uncharged atoms. Therefore, a plasma must be confined in some manner in order for us to have any chance of examining it. Due to the incredibly complex nature of their dynamics, however, the manner of confinement greatly influences how the plasma will behave, and tends to limit our understanding of plasmas to plasmas confined in the more common configurations. The most common method of confinement is the tokomak. This configuration has the plasma confined in the shape of a torus: a current passed through the core of the torus generates a toroidal field, a magnetic field whose field lines go the long way around the torus (Figure 1.1). A toroidal field tends to confine the plasma particles to helical orbits around the magnetic field lines. To counter the tendency of the particles to drift out of these orbits, a poloidal field, a magnetic field going the short way around, is also required for effective confinement. Current tokamaks are capable of plasma confinement lasting up to several seconds.

Although tokamak plasmas are the best understood, the limitations of the design have been recognized. For example, the central current requires significant power output to confine the plasma. The spheromak (Figure 1.1) is an alternative configuration. A spheromak is generated by ionizing hydrogen in a coaxial gun and then accelerating the plasma out into a container [4]. Spheromaks are toroidal plasmas confined with magnetic fields generated by the plasma itself, rather than by an external current. Although temperatures up to 400 electron volts (eV) have been reached, no spheromak has yet reached the tens of keV temperatures needed to initiate fusion. Spheromaks also have short lifetimes, a millisecond or less, since there is no power input during

the plasma's evolution.

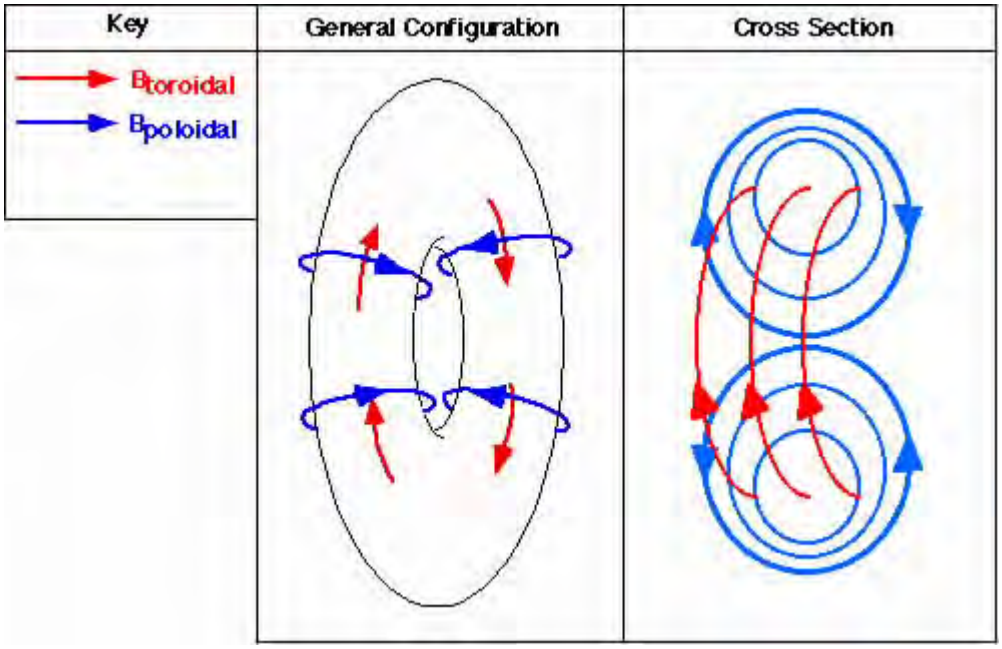

Figure 1.1: Schematic of a single spheromak showing poloidal (short way) and toroidal (long way) fields.

There are two principal ways to model plasma: a kinetic model and a fluid model. The kinetic model treats each particle separately, resulting in single particle orbits. These solutions are in 6-dimensional phase space, requiring six partial differential equations for each charged particle, as well as Maxwell's equations. Since a diffuse laboratory plasma might have 10^{19} m^{-3} particles and SSX-FRC has 10^{21} m^{-3}, the kinetic model is in practice only suitable for highly idealized and simple systems. Nevertheless, the kinetic model is of use for its ability to model processes that affect each individual particle in the plasma, such as particle drifts due to external fields and the resulting configurational stability.

The fluid model, on the other hand, only attempts to model gross properties of the system—pressure, temperature, mass density, and fluid velocity—by treating the plasma as a conducting fluid that responds to a $\mathbf{J} \times \mathbf{B}$ force. Moreover, since the formulation of this magnetohydrodynamic fluid model (MHD) encompasses Maxwell's equations, this approach greatly reduces the number of dynamic variables in the system and puts numerical simulations of laboratory plasmas within the reach of current computing capabilities. Modeling the plasma as a fluid also makes more tractable an examination of complex dynamics such as the propagation of waves and turbulence [14; 16].

Application of MHD leads to the realization that laboratory plasmas, and plasmas

in general, are prone to fluid phenomena that involve electromagnetic fields in novel ways. In an ideal MHD plasma, for example, magnetic flux lines are "frozen" to the fluid and move with it. Non-idealities in physical plasmas lead to phenomena such as magnetic reconnection, that is, the impossibility of maintaining an arbitrarily large magnetic field gradient in a region without some of the field lines "breaking" and reconnecting to field lines on the other side of the region. This reconnection, a topology change, leads to the conversion of magnetic energy to kinetic energy and is thought to be a principal energy source of energetic flows in solar coronal phenomena such as prominences, flares, and coronal mass ejections [3]. Reconnection is an integral part of SSX-FRC's operation: two spheromaks with antiparallel poloidal magnetic fields are allowed to come into contact (Figure 1.2). The toroidal fields cancel, but the antiparallel poloidal fields reconnect along the entire torus [28; 35]. The plasma is then said to be in a *field-reversed configuration* (FRC). This feature of SSX's design allows fundamental research on magnetic reconnection, hopefully leading to a more complete model that reflects the time and length scales observed in nature.

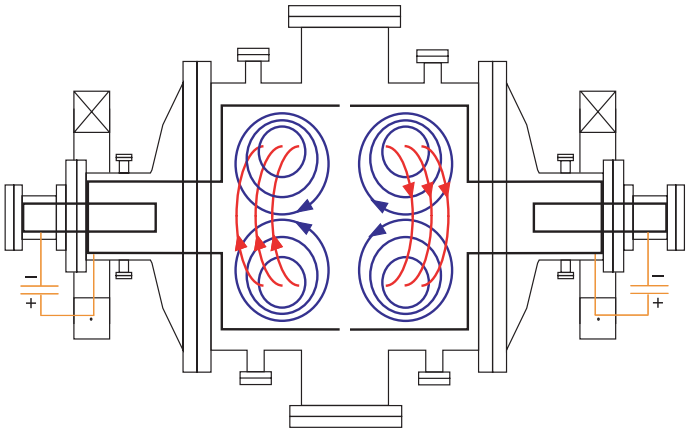

Figure 1.2: Two spheromaks about to merge inside SSX-FRC. Note the antiparallel poloidal fields that reconnect and the opposing toroidal fields that cancel.

This thesis will discuss the use of Ion Doppler Spectroscopy (IDS) to study plasma created and confined by SSX. Although the hydrogen used in SSX is 99.999% pure, the plasma liberates impurities from the vessel walls, particularly carbon [12]. Using an $f/9.4$ Czerny-Turner spectrometer, the IDS diagnostic will measure the location and width of the emission line of CIII at 229.7 nm [8; 15]. Since the carbon ions will be flowing at some velocity within the plasma, the line will be Doppler shifted from its rest location. Hence finding the centroid of the emission line will give us a measurement of the velocity of the plasma. The line will also have some finite width due to Doppler broadening, that is, the random thermal motions that will broaden the line due to the broader velocity distribution of particles at higher temperatures. This width is related to the ions' temperatures, so simply recording the emission line on a calibrated scale should give us both the velocity and the temperature of the ions

along the line of sight used [1; 20; 32].

Currently, however, the IDS system only uses 8 of the 32 total PMT's in the array. This means that the resolution of the system is low, being inherently unable to resolve any detail smaller than a single pixel width. As it currently stands, the minimum resolvable temperature is approximately 200 eV while the total temperature, the sum of ion and electron temperature, is expected to be approximately 30 eV [7]. The temperature measurements, however, do indicate a very wide line until the FRC is fully formed, at which point the linewidth drops to the minimum resolvable width. Our current thinking is that there is significant velocity shear due to the opposing reconnection jets that lead to the presence of multiple emission peaks due to the opposite Doppler shifts of the jets' emission lines. Their proximity then causes these emission peaks then overlap to make a single, double-peaked, distribution. Due to the IDS system's low resolution, the resulting data have the apprearance of a single, very wide and thus very hot, emission line. Since the lines are caused by reconnection, it would therefore make sense that the linewidth drop sharply when reconnection dies down. This phenomenon has not been seen before in a plasma IDS system because of the relatively recent development of PMT's with sufficiently high time resolution.

To investigate the shear hypothesis, I made a simple analytical model of a fluid system with velocity shear and determined the signal that an IDS system would get. The resulting signal is double-peaked, and in some cases the peaks are close enough together to appear to be a single, double-peaked, line. Although this model is simple, assuming purely azimuthal flows and a velocity varying only with radius, there is no reason to expect that the lineshapes it gives differ significantly from the lines in the real plasma. This model therefore does seem to confirm the hypothesis that velocity shear is responsible for the very wide emission line during the FRC formation, counter to the discussion in Ono et al. [28] that, while acknowledging the presence of significant velocity shear tied to magnetic reconnection, does not consider the possibility of velocity shear influencing the very high ion temperature values presented.

2 Single Particle Dynamics

The most productive line of inquiry regarding plasma motions is the fluid approach, which treats the plasma particles as a collective exhibiting fluid-like behavior (Sec 3). Nonetheless it is important to understand drifts, as bulk motions are called in the kinetic approach, when speaking of fluid flows. The kinetic approach to plasma physics described below takes each individual particle and applies the laws of electrodynamics to determine the likely behavior. While this method cannot be used to describe the full complexity of dynamics seen in plasmas due to computational requirements, it will tell us how the particles are moving in their flows for certain simple electromagnetic field configurations.

2.1 Helical Motion

The principal equation describing the dynamics of charged particles in fields is the Lorentz force law. In S.I. units, it is

$$m\mathbf{a} = q(\mathbf{E} + \mathbf{v} \times \mathbf{B}) \tag{2.1}$$

Let us now consider particle dynamics in a relatively straightforward case: zero electric field, and a constant magnetic field $\mathbf{B} = B_0\mathbf{b}$. In this case, the Lorentz force law is

$$\mathbf{a} = \frac{qB_0}{m}(\mathbf{v} \times \mathbf{b}) \tag{2.2}$$

Qualitatively, the acceleration is perpendicular to both the velocity and the magnetic field direction, so the motion perpendicular to the field is a circle in the plane. Parallel to the field the velocity is unaccelerated, so the motion is a straight line. The resultant motion of a moving particle in a constant magnetic field is therefore a helix centered on a magnetic field line (Figure 2.1) [10]. This result is exact for straight magnetic field lines and approximate for curved lines.

The quantity $\Omega = qB_0/m$ has units of s^{-1} and is called the *gyro-frequency*. The ratio of the velocity perpendicular to the field with the gyro-frequency gives the radius of the helix, the *gyro-radius* or *Larmor radius*.

$$\frac{v_\perp}{\Omega} = \rho_{gr} \tag{2.3}$$

2.2 ∇B drift

Previously, we assumed that the magnetic field was constant, an assumption that allows neither magnetic field gradients nor curved field lines. Let us now consider the case where the field has some gradient $\nabla\mathbf{B}$ [16].

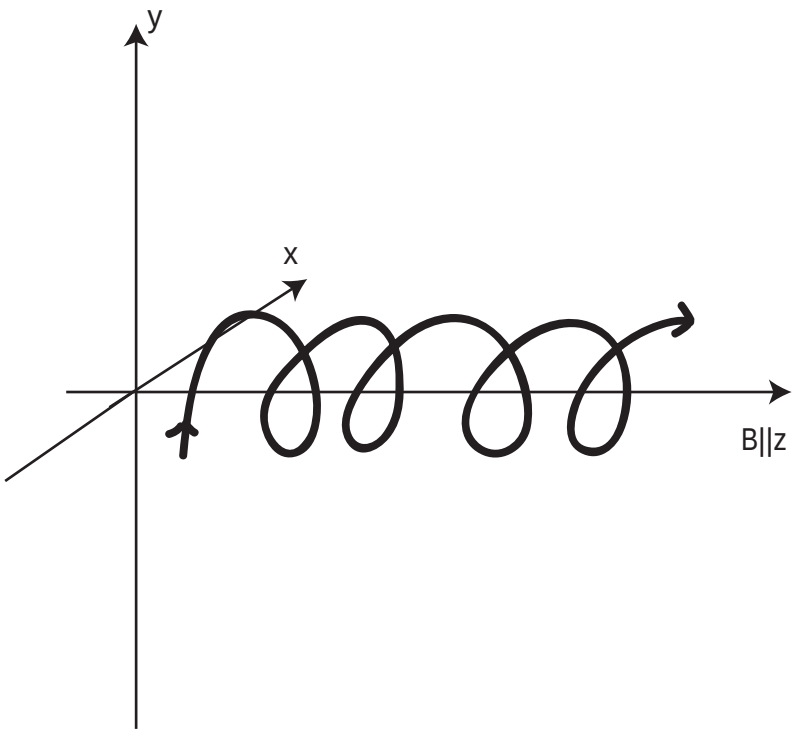

Figure 2.1: Helical motion of a charged particle along a magnetic field line.

When the particles orbit in the inhomogeneous **B**-field, the curvature of the orbit is greater where **B** is greater, causing a guiding center drift perpendicular to both **B** and $\nabla\mathbf{B}$ (Figure 2.2). The direction of the drift is dependant on the sign of the charge of the particle, so a $\nabla\mathbf{B}$ drift acts to separate particle species in a plasma such as the mostly proton-electron plasma in SSX.

Quantitatively, the derivation of the drift is found by decomposing the overall particle velocity into the sum of a guiding center velocity and an orbiting velocity. This is an approximation that requires the gyro-radius ρ_{gr} to be much smaller than the scaling in $\nabla\mathbf{B}$: $\rho_{gr} \ll \mid \mathbf{B}/\nabla\mathbf{B} \mid$. This then allows us to expand the **B**-field as a Taylor series and keep only the zeroth- and first-order terms:

$$\mathbf{B} \approx B_0 + (\rho_{gr} \cdot \nabla)\mathbf{B} \tag{2.4}$$

If we substitute this expression for **B** and the decomposed velocity into the Lorentz equation, eliminate products of first-order terms and average over the periodic variables $v_\perp$ and ρ_{gr}, we find the velocity of the guiding center to be

$$\mathbf{v_{gc}} = \frac{1}{q}\frac{mv_\perp^2}{2B}\frac{\mathbf{B} \times \nabla\mathbf{B}}{B^2} \tag{2.5}$$

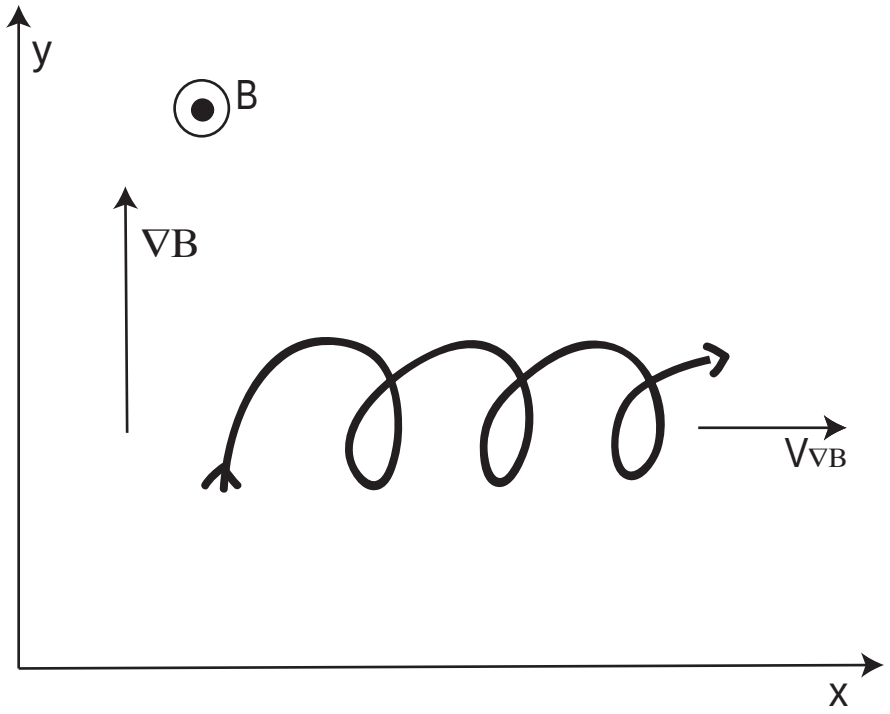

Figure 2.2: Guiding centre drift of a charged particle in the presence of a non-uniform magnetic field. The helix of Figure 2.1 points into the page, along the field line.

2.3 Stability of Toroidal Plasmas

Are toroidal plasmas stable? Clearly, a toroidal field alone has some confinement properties, the ideal behavior of a single charged particle being to continue along its field line forever. Unfortunately, given multiple particles with different charge signs, the different drifts prevent this. Since it is not possible to maintain an absolutely uniform magnetic field, the electrons and ions will move in opposite directions due to the $\nabla \mathbf{B}$ drift. This separation will induce a large electric field, and an $\mathbf{E} \times \mathbf{B}$ drift, qualitatively similar to the $\nabla \mathbf{B}$ drift will then expel both species outwards almost as fast as if there were no confining magnetic field (Figure 2.3). Although this effect is due to bulk motions of particle species, it still falls under the heading of kinetic plasma physics because it does not treat the plasma in terms of fluid variables.

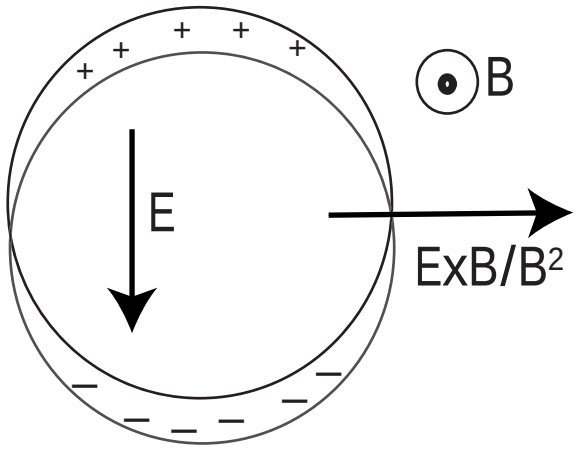

Figure 2.3: Separation of particle species inducing an $\mathbf{E} \times \mathbf{B}$ force.

So a toroidal field alone is not sufficient to confine the particles. It turns out that the addition of a poloidal magnetic field B_θ, so that the field lines become helical and wind around the torus, can be sufficient for confinement [10].

3 Magnetohydrodynamic Plasma Physics

3.1 Ideal MHD

As the number of particles in a plasma increases and the dynamics become more complex, the kinetic approach to plasma modeling is no longer effective. In an SSX plasma, particle densities are often around $10^{21}\ m^{-3}$. Rigorously solving for each particle's motions would require 6 partial differential equations for each particle, as well as Maxwell's equations. In a system with so many particles, this is not a feasible approach. *Magnetohydrodynamics*, or MHD, is a more applicable model that treats the plasma as a conducting fluid by combining the equations of fluid dynamics with Maxwell's equations. In the MHD model, plasmas have eight gross fluid variables: mass density ρ, plasma pressure $p = nkT$ (the plasma may be considered an ideal gas in thermal equilibrium), velocity $\mathbf{v}$ and current density $\mathbf{J}$. There are also the six field variables: magnetic field $\mathbf{B}$ and electric field $\mathbf{E}$.

The corresponding ideal MHD equations are [14]

the time evolution of mass (continuity equation):

$$\frac{\partial \rho}{\partial t} + \nabla \cdot \rho \mathbf{v} = 0 \tag{3.1}$$

the time evolution of energy:

$$\frac{d}{dt}(\frac{p}{\rho^{\gamma}}) = 0 \tag{3.2}$$

the time evolution of momentum:

$$\rho \frac{\partial \mathbf{v}}{\partial t} = \mathbf{J} \times \mathbf{B} - \nabla p \tag{3.3}$$

Ohm's Law for a perfect conductor:

$$\mathbf{E} + \mathbf{v} \times \mathbf{B} = 0 \tag{3.4}$$

the pre-Maxwell equations

$$\nabla \times \mathbf{B} = \mu_0 \mathbf{J} \tag{3.5}$$

$$\nabla \times \mathbf{E} = -\frac{\partial \mathbf{B}}{\partial t} \tag{3.6}$$

$$\nabla \cdot \mathbf{B} = 0 \tag{3.7}$$

It is worth noting that a comprehensive measurement of $\mathbf{v}$ such as the IDS systems sets out to do would eliminate three of the eight fluid variables from the equations,

and that $\mathbf{v}$ is found in all the non-electrodynamic MHD equations bar the energy equation.

There are several conditions that a plasma must meet for ideal MHD to apply. First, it must be strongly magnetized. This has the effect of restricting the gyroradius ρ_{gyro} of the particles, so that $\rho_{gyro} \ll L$, where L is a characteristic length scale of the system. This condition ensures that plasma motions are similar to those of fluid elements in conventional fluids. Second, an MHD plasma cannot be dissipative: it must have slow transport rates due to dissipation as compared to other energy transport timescales. Third, the plasma must be quasi-neutral. That is, the plasma must be electrically neutral over some scale—*the Debye length*—that is small compared to other characteristic length scales in the system. Hence any violations of charge neutrality are local rather than global [16]. In reality, the third condition is universally true of objects considered to be plasmas and it can be taken as an alternative definition of plasma [3].

These conditions make terms in Ohm's law so small that the plasma Ohm's Law can be in many situations taken to be $\mathbf{E} + \mathbf{v} \times \mathbf{B} = 0$. This describes a system with infinite conductivity, and so this approximation is only valid when the plasma has very small resistivity. A plasma for which this is true is an ideal plasma, the MHD theory that assumes this is "ideal MHD".

3.2 Alfvén's Theorem

The approximation of infinite conductivity leads to one of the most important effects in plasma physics, the "frozen-in flux theorem", or Alfvén's Theorem. This theorem states that when $\mathbf{E} + \mathbf{v} \times \mathbf{B} = 0$, the plasma and the magnetic field lines are tied together, and when one moves, the other must necessarily more with it. The derivation follows Goldston [16].

First of all, we can show that the magnitude of magnetic flux through any closed contour (Figure 3.1) that moves with the plasma is constant.

The induction equation (Faraday's Law) states that

$$\frac{\partial \mathbf{B}}{\partial t} = -\nabla \times \mathbf{E} \tag{3.8}$$

Given our approximation of infinite conductivity, we get

$$\frac{\partial \mathbf{B}}{\partial t} = \nabla \times (\mathbf{v} \times \mathbf{B}) \tag{3.9}$$

Now the definition of magnetic flux is the integral of $\mathbf{B}$ over some area.

$$\Phi = \int \mathbf{B} \cdot d\mathbf{s} \tag{3.10}$$

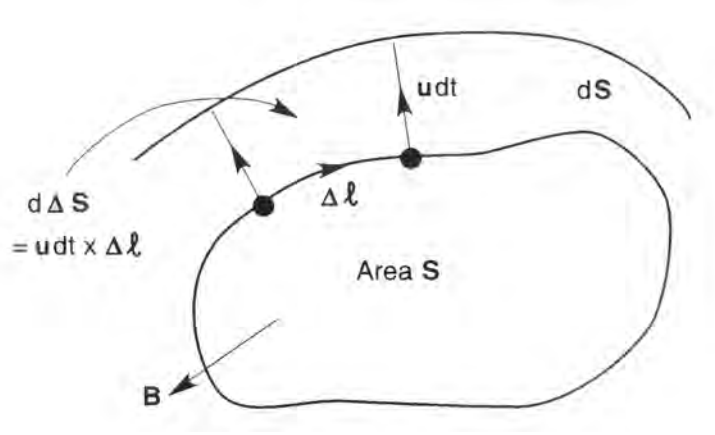

Figure 3.1: A closed contour evolving with time.

The rate of change of the flux is therefore due to both the change in the time-dependent magnetic field and the change in the area bounded by the contour.

$$\frac{d\Phi}{dt} = \int \nabla \times (\mathbf{v} \times \mathbf{B}) \cdot d\mathbf{s} + \int \mathbf{B} \cdot \frac{d(\triangle \mathbf{s})}{dt} \tag{3.11}$$

From Stokes' Theorem for curls,

$$\int (\nabla \times (\mathbf{v} \times \mathbf{B})) \cdot d\mathbf{s} = \int (\mathbf{v} \times \mathbf{B}) \cdot d\mathbf{l} \tag{3.12}$$

where $\mathbf{d}$l is some element of the boundary of the contour. From the geometry of the system, however, we see that since $d(\triangle \mathbf{s}) = \mathbf{v}dt \times d\mathbf{l}$,

$$\frac{d(\triangle \mathbf{s})}{dt} = \mathbf{v} \times d\mathbf{l} \tag{3.13}$$

Therefore, the change in the flux is

$$\frac{d\Phi}{dt} = \int \mathbf{v} \times \mathbf{B} \cdot d\mathbf{s} + \int \mathbf{B} \cdot (\mathbf{v} \times d\mathbf{l}) = 0 \tag{3.14}$$

So the flux through any contour "painted" on the plasma does not change with time in ideal MHD.

Unchanging flux also implies that the plasma and the field are frozen together. The argument is as follows: Consider a tube of plasma surrounding some field line. Since no field line pierces the tube (we neglect the ends of the tube), the flux through it is zero. As time passes, the flux remains zero due to the previous theorem. This implies that at no time during the evolution of the field line does it pierce the tube. Hence, the tube must move with the line at all times.

3.3 Magnetic Reynolds number

The frozen-in field effect technically only occurs in ideal MHD plasmas whose conductivities are infinite. Since no real-world plasma is ideal in this sense, some quantitative way of judging the "ideal"-ness of a plasma is needed. This is the motivation for the magnetic Reynolds number. Since in an ideal plasma with zero resistivity the field is tied to the flow, diffusion of the plasma across the field as the field changes is not possible.

The change in the field is given by the induction equation

$$\frac{\partial \mathbf{B}}{\partial t} = -\nabla \times \mathbf{E} = \nabla \times (\mathbf{v} \times \mathbf{B}) + \frac{\eta}{\mu_0} \nabla^2 \mathbf{B} \tag{3.15}$$

The first term on the right is the movement of the field with the fluid while the second term describes the field moving perpendicular to the fluid, a diffusive motion. The magnetic Reynolds number is the dimensionless ratio of the convection to the resistive diffusion and can be expressed as

$$R_M = \frac{\mu_0 v L}{\eta} \tag{3.16}$$

for a plasma with resistivity η, velocity v and characteristic length scale L. The infinite-conductivity approximation is therefore valid for large values of R_M. Hence it seems that the greater the plasma's velocity, the closer to ideal MHD its behavior becomes, making velocity an important factor in how a plasma will behave. SSX-FRC has a Reynolds number of approximately 10^2–10^3. This is significantly smaller than the numbers of comparable natural astrophysical plasmas—solar flares, for example, have Reynolds numbers in the range of 10^9–10^{14} [17].

3.4 Beta

To some extent, the large external magnetic fields used to confine laboratory plasmas are unnatural. In many astrophysical plasmas hydrodynamic properties such as pressure and temperature contribute significantly to confinement, and magnetic fields, while oftentimes necessary, are of less importance. Laboratory plasmas, on the other hand, employ very strong magnetic fields that are generated externally to produce a pressure on the plasma. These fields require significant expenditures of power to maintain and make for plasmas that differ significantly from astrophysical plasmas. A useful measure of the relative importance of the magnetic field in plasma confinement is beta β. This dimensionless quantity is defined to be the ratio of the plasma pressure p to the magnetic field pressure where $p = nk_BT$ since plasmas can be considered to be ideal gases.

$$\beta = \frac{2\mu_0 p}{B^2} = \frac{2\mu_0 n k_B T}{B^2} \tag{3.17}$$

Therefore the hotter the plasma, the greater the magnetic field pressure required for confinement. Typical astrophysical plasmas have values of beta ranging anywhere from 10^{-3} in the case of the solar corona, to values on the order of unity for hot diffuse interstellar plasmas. Magnetized laboratory plasmas have betas less than unity. Typical values range from approximately 0.05 for tomamaks to the high end of 0.1 for spheromaks such as SSX produces. Spheromaks have similar betas to solar flares, whose betas range from 0.01 to 0.1. Like R_M, β shows the importance of the plasma parameters measured by an IDS diagnostic.

4 Magnetic Reconnection and SSX-FRC

4.1 Magnetic Reconnection

Magnetic reconnection is a phenomenon that occurs in nonideal magnetized plasmas. It is the primary mechanism for the conversion of magnetic energy to kinetic and thermal energy in such plasmas. Imagine the following scenario: Two "slabs" of magnetized plasma, with oppositely directed magnetic fields, come into contact with their motion perpendicular to their magnetic field vectors (Figure 4.1A, 4.1B).

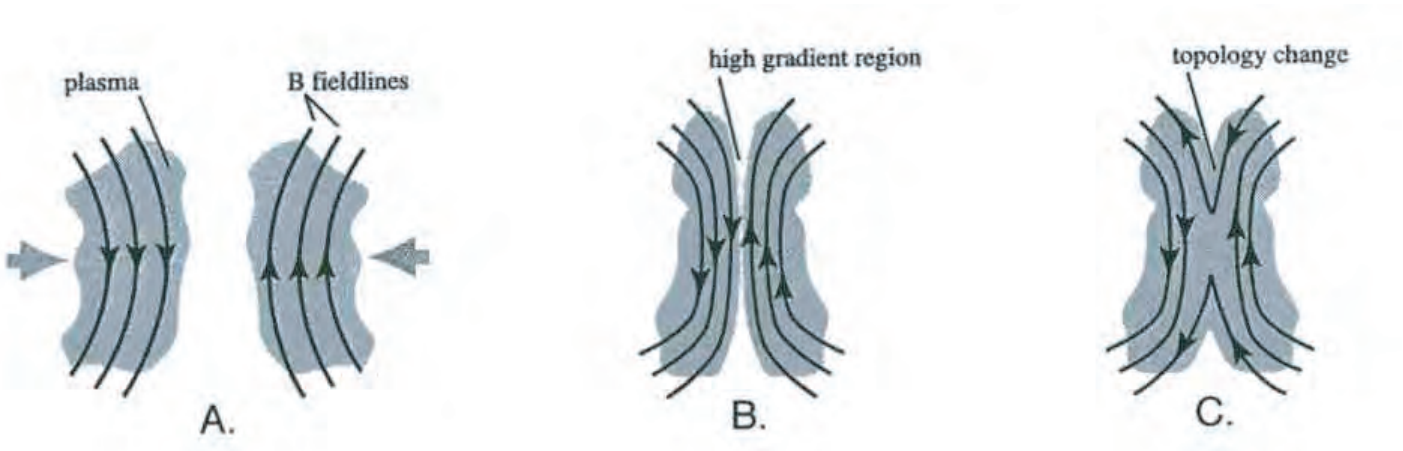

Figure 4.1: The stages leading (A, B) to magnetic reconnection (C).

In an ideal magnetohydrodynamic plasma with zero conductivity η, there are no further dynamics. However, in a non-ideal plasma, η is small but non-zero. Since the curl of the magnetic field is large around the region of contact (Figure 1B), a large electric current **J** is generated by Ampère's Law, Equation 3.5. The finite η allows for collisional dissipation across the current sheet, resulting in the annihilation of magnetic flux. This leaves the reconnection region unmagnetized, so there form two oppositely directed heated jets leaving the reconnection region parallel to the magnetic fields. This loss of magnetization due to the destruction of flux can be thought of as "reconnection" of magnetic field lines across the boundary between the two slabs (Figure 1C). Reconnection can be seen to cause the movement of plasma across the fieldlines. The annihilation of flux and the movement across the field-lines is a local decoupling of field and plasma and hence a violation of the frozen-in flux/field' condition of ideal MHD plasmas [3; 24; 25].

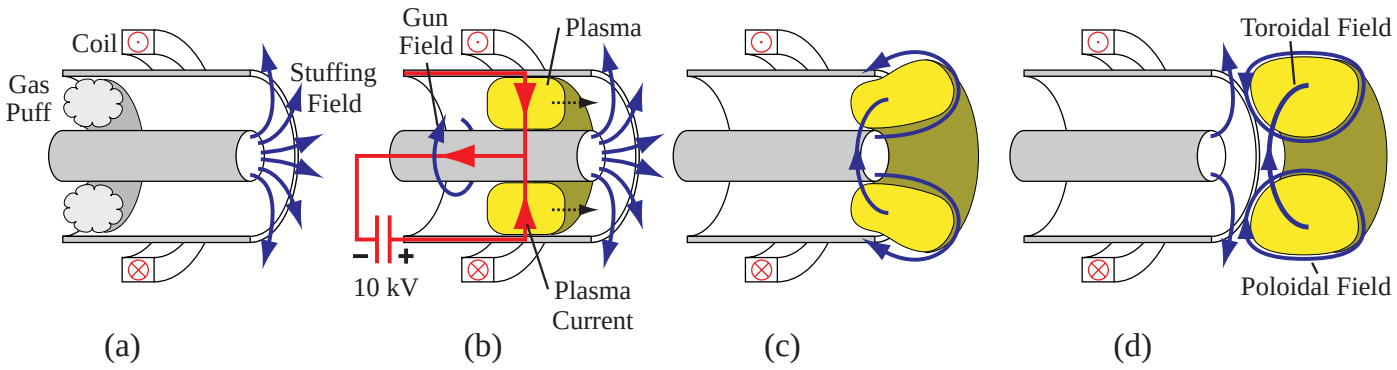

Figure 4.2: Spheromak formation using a coaxial magnetized plasma gun.

4.2 Spheromaks

The particular plasma configuration seen in SSX is a result of the method of production, which uses the coaxial magnetized plasma gun. The formation process is shown in Figure 4.2. Initially, there is a vacuum poloidal field that connects the innder and outer electrodes (Figure 4.2A). This field is called the *stuffing flux*. To provide the material for the plasma, fast valves inject hydrogen gas into the gun. This gas is made plasma when a capacitor bank to applie high voltage across the electrodes, ionizing the hydrogen (Figure 4.2B). Since the plasma is a good conductor, the impedance between the electrodes drops nearly to zero, effectively resulting in a short circuit. The plasma accelerates through the gun, and when the plasma encounters the stuffing flux, the frozen-in flux condition couples the two together. The plasma blows the field out of the gun like a soap bubble (Figure 4.2C), twisting the field lines. When the plasma has twisted the field enough, reconnection occurs at the gun end, detaching the spheromak (Figure 4.2D) whose magnetic structure is a set of nested flux surfaces [4].

Mathematically, a spheromak is a particular equilibrium solution of the MHD equations (Equations 3.1–3.7). Auerbach [1] gives a straighforward physical derivation. Beginning with the MHD equation for momentum, Equation 3.3,

$$\rho \frac{d\mathbf{v}}{dt} = \mathbf{J} \times \mathbf{B} - \nabla p$$

we seek an equilibrium configuration for the plasma. In such a state, called a "force-free" state, we expect that all forces on the plasma balance. Hence we can set both sides of Equation 3.3 to zero, allowing us to write

$$\mathbf{J} \times \mathbf{B} = \nabla p = 0 \tag{4.1}$$

The second equality holds because of the experimental fact that spheromaks have low β [5], so $P \ll B^2$. This means that the magnetic field and the current are parallel,

which makes physical sense since the current is toroidal and spheromak has a toroidal magnetic field. If the current and field are parallel, then the vectors are related by $\mathbf{J} = \lambda\mathbf{B}$ for some scalar λ. Hence by the Maxwell equation $\nabla \times \mathbf{B} = \mu_0\mathbf{J}$, we have the equation for a force-free state, or *Taylor state*

$$\nabla \times \mathbf{B} = \lambda\mathbf{B} \tag{4.2}$$

From Equation 4.2, there is a simple proof by contradiction that shows the existence of flows, even in the steady state. First let us assume zero flow and a steady state. Then Ohm's Law

$$\mathbf{E} = (\mathbf{v} \times \mathbf{B}) + \eta\mathbf{J} = \eta\mathbf{J} \tag{4.3}$$

since $\mathbf{v} = 0$. Taking the curl of Equation 4.3, we get

$$\nabla \times \mathbf{E} = \nabla \times \eta\mathbf{J} \tag{4.4}$$

Taking the curl of Equation 3.5 and dropping the constant μ_0, we get

$$\nabla \times \mathbf{J} = \nabla \times (\nabla \times \mathbf{B}) \tag{4.5}$$

which we can rewrite using the equation for a Taylor state, Equation 4.2, as

$$\nabla \times \mathbf{J} = \nabla \times (\lambda\mathbf{B}) = \lambda^2\mathbf{B} \tag{4.6}$$

Using Equation 4.4 and again dropping the constant we have

$$\nabla \times \mathbf{E} = \lambda^2\mathbf{B} \tag{4.7}$$

However, since we are in the steady-state, $\nabla \times \mathbf{E} = 0$ by Faraday's Law (Equation 3.6). But $\mathbf{B}$ is nonzero, so we have a contradiction. The resolution to the contradiction is to accept that $\mathbf{v} \neq 0$.

4.3 Field Reversed Configuration (FRC)

SSX-FRC does not study single spheromaks. Following Ono et al. [28], SSX collides two spheromaks with oppositely directed toroidal fields. Figure 4.3 is a cross-section of SSX-FRC showing the magnetic structure within. Since the poloidal fields are antiparallel, they reconnect. The toroidal fields, however, are oriented so that instead of reconnecting, they annihilate. Ideally a merger of spheromaks would create a configuration with zero toroidal field, or an FRC. However, some residual toroidal field remains, so SSX-FRC forms a plasma configuration properly called a *hybrid FRC* [13]. Typical SSX-FRC parameters are 3-4 mWb poloidal flux, 30 eV total temperature, 1kG magnetic field, and 10^{15} cm^{-3} particles [7].

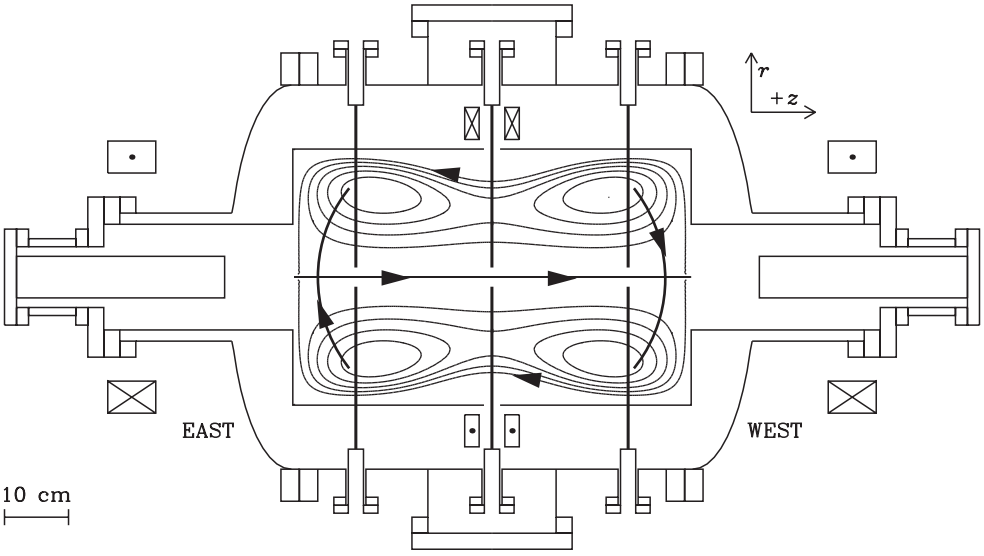

Figure 4.3: SSX-FRC.

The reconnection region shows the location of the jets (Fig 4.4). The poloidal field reconnection drives oppositely-directed radial jets along the midplane, and the residual toroidal field, even after the FRC has formed and reconnection has stopped, should also contribute to this current. The drive for these flows comes from the $\mathbf{J} \times \mathbf{B}$ force. As the radial currents cross the poloidal fieldlines, a $\mathbf{J} \times \mathbf{B}$ force results. As the direction of the poloidal field changes, however, so should the direction of this force. Hence a torque is set on the system, which drives the radial jets.

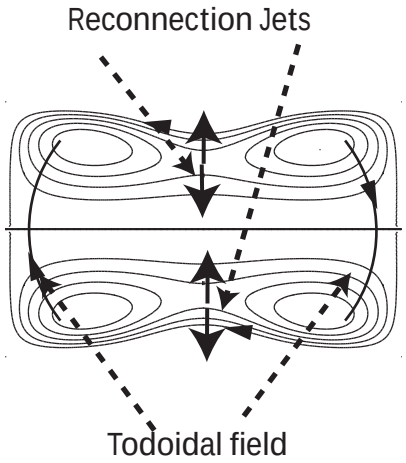

Figure 4.4: Jets from the reconnection region.

4.4 FRC Geometry

The geometry of an FRC can be investigated using pressure balance [33]. By assuming a cylindrical FRC with straight magnetic field lines at the midplane, the maximum plasma pressure can be expressed as

$$P_{max} = P(\psi) + \frac{B_z^2}{2\mu_0} \tag{4.8}$$

where $\psi = \int B_z r dr$, the poloidal flux. Hence $d\psi/B_z = rdr$. This implies that ψ is a symmetric function $\psi = \psi(r^2 - R_0^2)$, where R_0 is the field null or location where the polar field is zero. Therefore, all functions of ψ must vary symmetrically with $r^2 - R_0^2$. This allows us to find R_0 since the integral of rdr must be equal whether it is from 0 to R_0 or from R_0 to R_{max}. Integrating, we get

$$R_0 = \frac{R_{max}}{\sqrt{2}} = 0.7071 R_{max} \tag{4.9}$$

In a configuration such as SSX-FRC, R_{max} is the vessel wall and R_0 is the vessel's centreline. The value of Eq. 4.9 is that it tells us that the field null of an FRC lies closer to its container's wall than to the centre. As Figure 4.4 demonstrates, the field null is the obvious site for reconnection-driven jets and therefore its non-medial position must be taken into account when trying to determine or model a flow profile (Section 8). Experiment shows that Equation 4.9 is approximately correct for SSX-FRC. With a 40 cm diameter and hence $R_0 = 20$cm, Cothran et al. [7] show that the null occurs at $r = 13$cm, very close to $R_0/\sqrt{2} = 14.1$cm.

5 Diffraction and Spectroscopy

The previous Sections have attempted to explain and motivate the basic plasma physics behind SSX-FRC. This section will detail the optical and spectroscopic principles underlying the Ion Doppler Spectroscopy (IDS) diagnostic, with the aim of showing how such a diagnostic might be used to investigate the jets and flows previously mentioned. Arising from the wave character of light, the most fundamental phenomena in this regard are interference and diffraction. Explaining the diffraction grating will show how these phenomena are used to produce a spectrum of light and what the characteristic properties of gratings are that affect the spectra they produce. Moreover, the diffraction grating used by SSX-FRC's IDS diagnostic is an *echelle* grating and so its properties differ from the more commonly used gratings. Of course, the grating is not used on its own, but is mounted in a spectrometer to direct the light onto the grating and from the grating onto an imaging plane. SSX-FRC uses a Czerny-Turner (CZ) spectrometer. Finally, the phenomenon of Doppler shift of light is discussed, to understand how we can determine velocity and temperature from the spectrum.

5.1 Interference and Diffraction

When two waves originally from a single source are combined at a point, the resultant intensity depends upon the relative phase of the waves at that point. If the waves are in phase, an extremum of one will add with a similar extremum of the other, resulting in constructive interference. If, on the other hand, the phase difference is such that the amplitudes of the waves are opposite, destructive interference will be the result and the waves will cancel each other out at that point. A simple system that illustrates this behavior is single-slit diffraction. The following analysis is taken from Pedrotti et al. [31].

A source is placed behind a screen cut with a single slit of finite with b, projecting an image onto a screen (Figure 5.1). Huygens' Principle allows us to consider the slit as an array of spherical wavelet sources, propagating forward. Each infinitesimal interval ds of the slit will contribute a spherical wavelet at a given point p on the screen of form

$$dE_p = \frac{dE_0}{r} e^{i(kr-\omega t)} \tag{5.1}$$

where r is the optical pathlength from ds to p.

Integrating over the entire width of the slit b, we find the irradiance pattern on the screen to be a sinc-squared function called the diffraction function (Figure 5.2).

$$I = I_0 (\frac{\sin \beta}{\beta})^2 \tag{5.2}$$

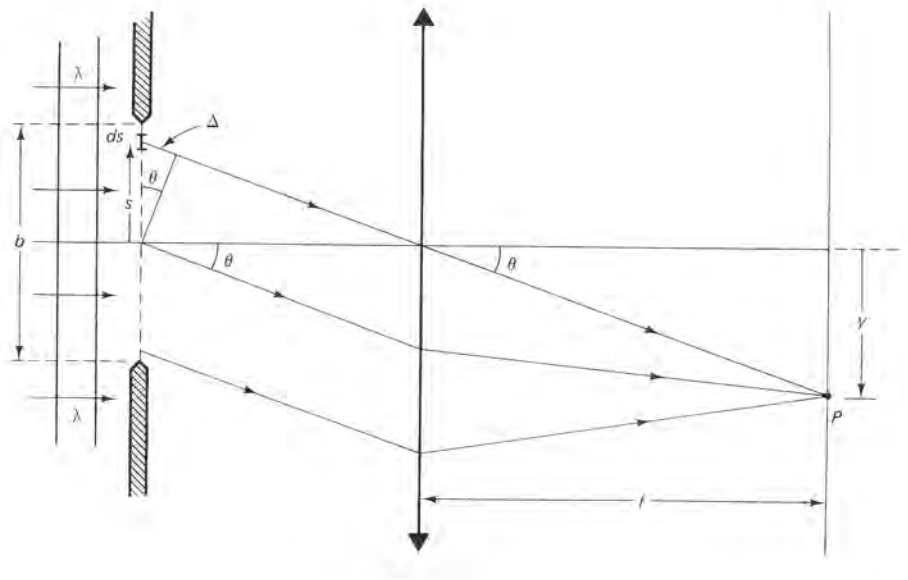

Figure 5.1: Single-slit diffraction.

$$\beta = \frac{1}{2}kb\sin\theta = \frac{\pi b}{\lambda}\sin\theta \tag{5.3}$$

The irradiance pattern is symmetrical about, and has a central maximum at, $\theta = 0$. It has recurring minima at

$$m\lambda = b\sin\theta \tag{5.4}$$

5.2 Diffraction Gratings

The above result, the irradiance due to a screen with one slit, can be generalized to a screen with N slits. When N is large, the screen is properly called a diffraction grating. There are two types of grating: transmission gratings that are essentially equivalent to the slitted screen idealized above; and reflection gratings, whose slits' are in fact reflective grooves ruled on the grating's surface. Although with regard to interference effects the physics of the two kinds of grating are identical, reflection gratings are by far the more common type used in spectroscopy. SSX's IDS spectrometer uses a reflection grating.

The irradiance due to a diffraction grating with N reflecting grooves of width b and groove spacing a is derived similarly to the single-slit grating, except that the limits of integration are changed so that the initial integral is a series of N terms.

$$E_R = \frac{E_L}{r_0}\sum_{j=1}^{N/2}\left(\int_{[-(2j-1)a-b]/2}^{[-(2j-1)a+b]/2} e^{isk\sin\theta}ds + \int_{[(2j-1)a-b]/2}^{[(2j-1)a+b]/2} e^{isk\sin\theta}ds\right) \tag{5.5}$$

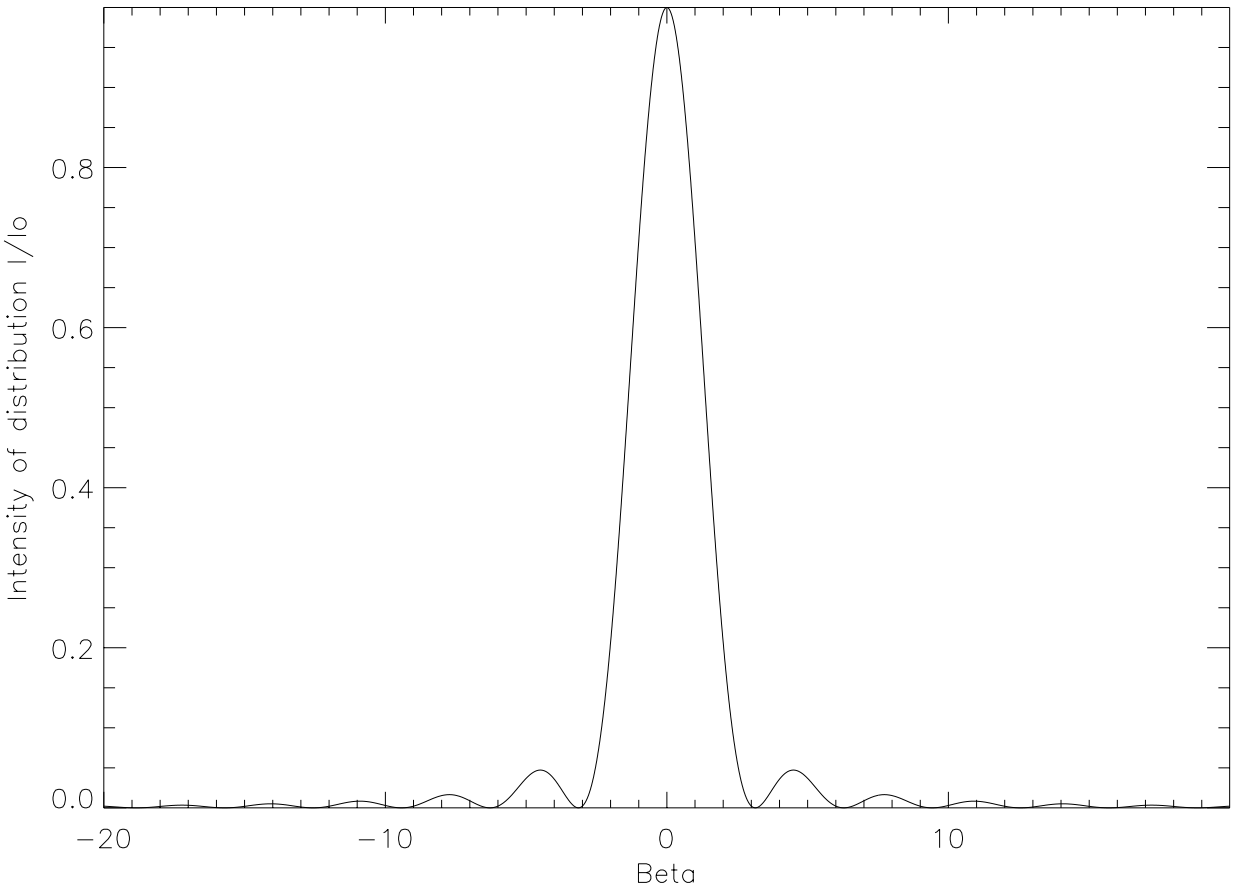

Figure 5.2: Diffraction function: variation of light intensity across an image plane for a single slit.

Calculating the sum and taking the square of the resulting amplitude gives the irradiance pattern on the screen:

$$I = I_0(\frac{\sin\beta}{\beta})^2(\frac{\sin N\alpha}{\sin\alpha})^2 \tag{5.6}$$

$$\alpha = \frac{1}{2}ka\sin\theta = \frac{\pi a}{\lambda}\sin\theta \tag{5.7}$$

$$\beta = \frac{1}{2}kb\sin\theta = \frac{\pi b}{\lambda}\sin\theta \tag{5.8}$$

The $(\sin\beta/\beta)^2$ factor is the same diffraction function as in the single-slit case. The $(\sin N\alpha/\sin\alpha)^2$ factor, called the interference function, has maxima when

$$m\lambda = a\sin\theta \tag{5.9}$$

where m is called the *order* of the peak.

The combination of the interference function with the diffraction function results in the maxima of the interference function being attenuated by the diffraction function, which becomes an envelope (Figure 5.3).

The total interference pattern (Figure 5.3) has the same conditions for minima as the interference function (Equation 5.9). Since the total interference pattern is the output of a diffraction grating, Equation 5.9 is called the diffraction grating equation since it gives peak locations, if not their magnitudes.

However, the light reaching the screen in the case of a reflection grating does not come from a source behind the grating and therefore has both an angle of incidence θ_i and an angle of reflection θ_r (Figure 5.4). The diffraction grating equation may be modified if we realize that a statement equivalent to the grating equation would be that the optical path-length difference between two rays of light must equal some integer multiple of the wavelength for there to be constructive interference.

From trigonometry, the grating equation for a reflecting diffraction grating must be

$$m\lambda = a(\sin\theta_i - \sin\theta_r) \tag{5.10}$$

What this means is that for light incident at a particular angle θ_i, the reflection angle θ_r depends on the light's wavelength λ. A diffraction grating therefore takes incident light and images a series of peaks, each series corresponding to one component wavelength of the light. If we focus on a region close to one of the peaks, the image is a spectrum of the component wavelengths in the light with intensity as a function of wavelength.

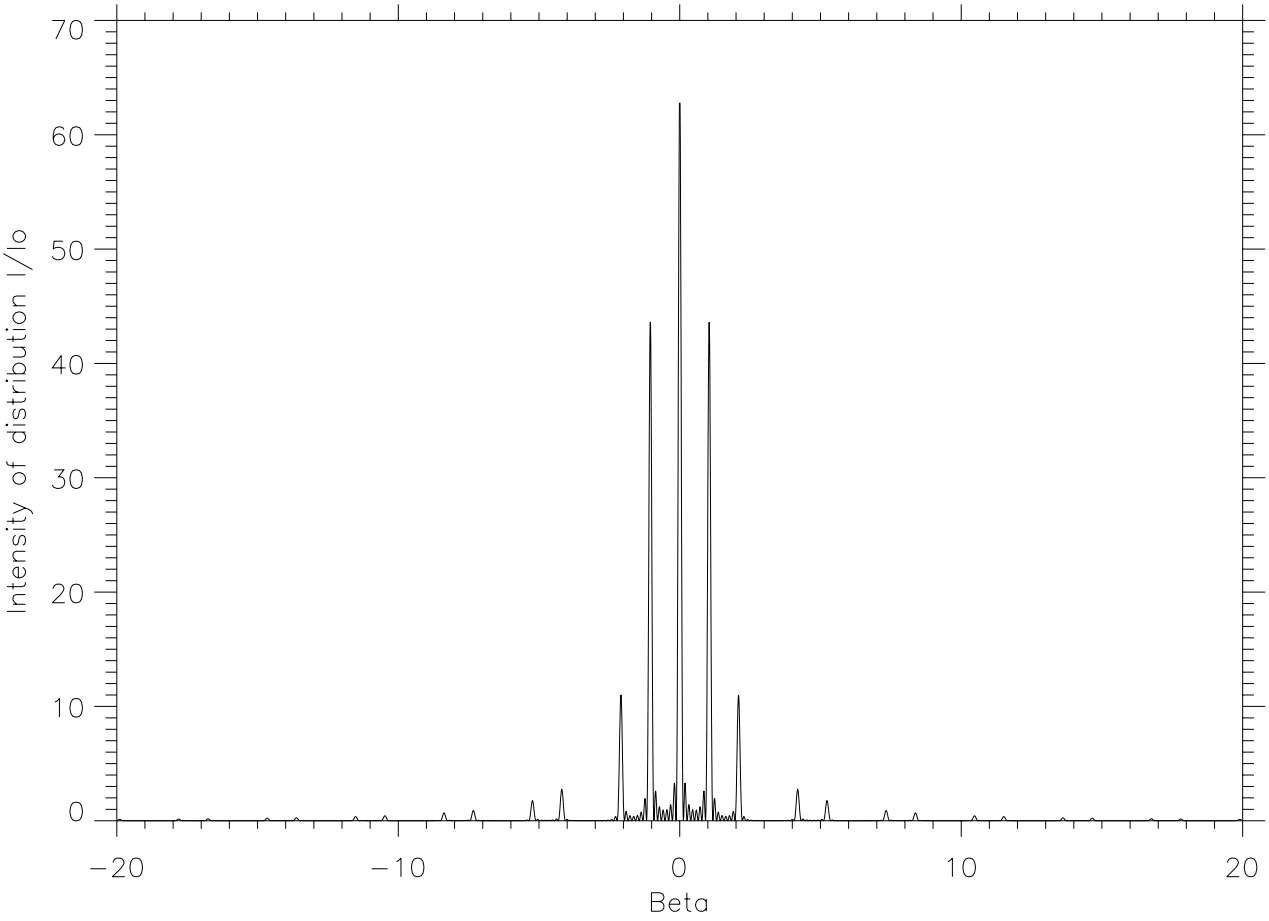

Figure 5.3: Attenuation of the interference maxima due to the diffraction envelope.

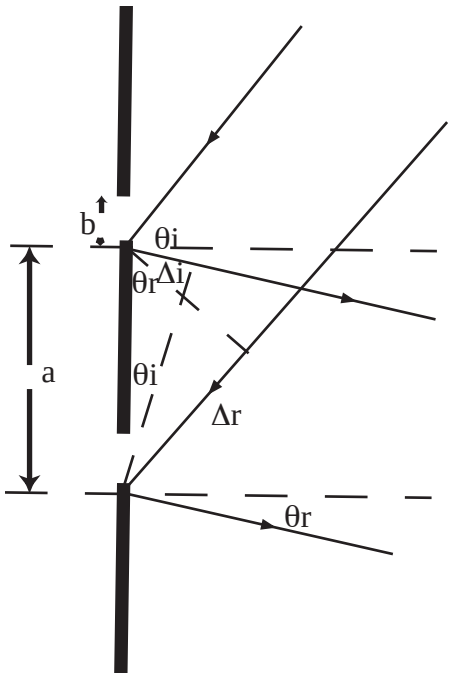

Figure 5.4: Geometry of a diffraction grating: the △'s are the optical path-length differences.

5.3 Dispersion of a grating

Although every diffraction grating creates a spectrum, the usefulness of the spectrum depends on how much information can be taken from it. If the peaks are very close together, then it will be more difficult to use. The measure of "distance" across the image of a spectrum is a measure of the angular separation of wavelengths in the spectrum, called the *angular dispersion* D.

$$D \equiv \frac{d\theta_r}{d\lambda} \tag{5.11}$$

which the grating equation allows us to rewrite as

$$D = \frac{m}{a \cos \theta_r} \tag{5.12}$$

The linear dispersion is the variation in wavelength along the length of the imaging screen $dy/d\lambda$ and is just

$$fD = \frac{fm}{a \cos \theta_r} \tag{5.13}$$

since $dy = f d\theta_r$ (Fig 5.5) where f is the focal length of the mirrors in the spectrometer (Section 5.7).

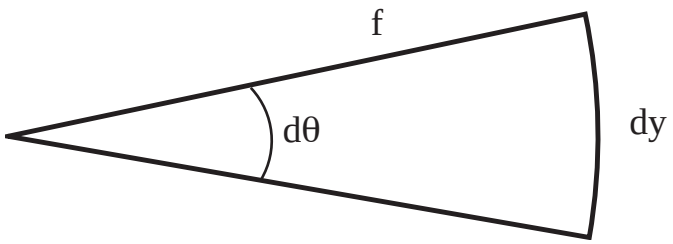

Figure 5.5: Relationship between angular and spatial separation.

5.4 Resolution of a grating

The dispersion of the spectrum tells us only how spread out it is, nothing about the distinctness of neighboring peaks. The resolving power R of a grating, defined as

$$R \equiv \frac{\lambda}{\triangle\lambda_{min}} \tag{5.14}$$

is the property of the grating that determines the sharpness of the spectrum. Quantifying R is usually done by accepting Rayleigh's criterion for the resolution of peaks, that is, that two adjacent peaks are just barely resolvable if the maximum of one coincides with the first minimum of the other in the same order. Although Rayleigh's criterion is somewhat arbitrary in that it specifies a minimum resolvable separation of peaks, it is still useful and allows us to quantify resolving power, as well as determining its dependences. Using the grating equation in conjunction with this criterion, the theoretical resolving power is found to be

$$R = mN \tag{5.15}$$

where N is the total number of grooves on the diffraction grating.

5.5 Echelle Gratings

Since the IDS diagnostic aims to measure the position and width of a single spectral line, there are several optical characteristics to be considered. If the diagnostic is to be precise, maximizing resolution and dispersion is a must. From Equations 5.13 and 5.15 it can be seen that the ideal dispersing element would be finely ruled to minimize a and maximize N, and would operate at large reflection angles and at high interference order. The best compromise to this ideal is the echelle grating. An echelle is a coarsely ruled diffraction grating designed only for use at high order and high diffraction angles. Typically, an echelle will have 316 grooves/mm or less, operate at very high orders— up to 600th in the most extreme cases— and have angles of more than 60°. The echelle grating used in the IDS system has 316 grooves/mm

and is used at 25th order. In comparison, a regular grating will have around 3000 grooves/mm and operate at less than fifth order. Given these parameters, SSX's 1.3 m spectrometer with an echelle grating has the same dispersion as a 5 m spectrometer with a normal grating made to work at first order.

The principal feature of the echelle that leads to these characteristics is its grooves. Echelles are blazed (Figure 5.6); that is, each groove is triangular, with a characteristic facet angle ϕ. The difference between an echelle grating and a normal blazed grating, however, is that echelles reflect from the narrow edge of the groove, leading to high reflection angles that give the grating a large dispersion (Equation 5.13).

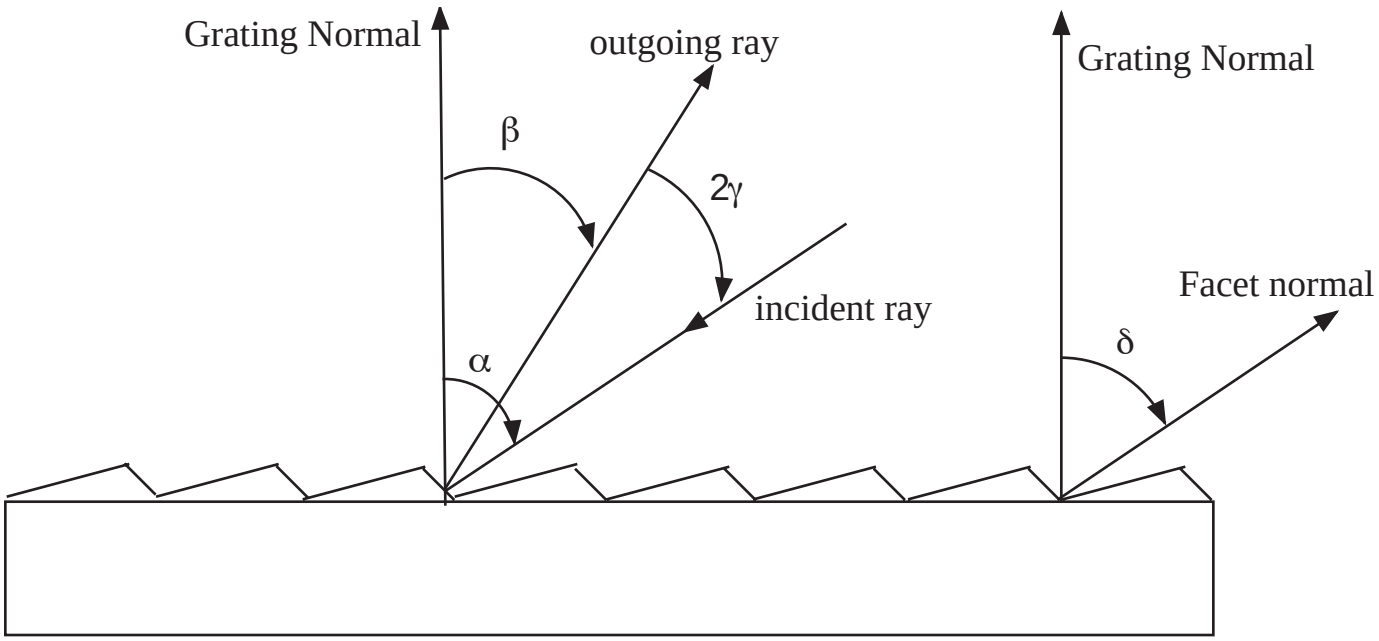

Figure 5.6: Geometry of an echelle grating.

As well as leading to high angles, the blaze is what allows the echelle to be operated at high order. Like all gratings, the intensity pattern from an echelle is a combination of a regular interference pattern with a diffraction envelope attenuating the intensity with distance from the central maximum. Normally, the central diffraction maximum coincides with the zeroth interference order. This means that most of the light energy goes into the low orders, where dispersion and resolution are small, and makes the higher, more useful, orders imperceptibly faint. Blazing the grating causes the diffraction envelope to be centered at some higher order, making spectral analysis much easier. The angle between the $m = 0$ light beam and the $\beta = 0$ light beam to the center of the diffraction pattern is called the blaze angle, and is approximately equal to the facet angle [27].

5.6 Thin-Lens Systems

A thin lens is a lens whose thickness is small compared to the distance from the lens to the image. Assuming lenses to be thin greatly simplifies the analysis of lens systems. The primary equation of thin lenses is

$$\frac{1}{I} + \frac{1}{O} = \frac{1}{f} \tag{5.16}$$

where O is the distance from the lens to the object, I is the distance from the lens to the image, and f is the focal length of the lens. The meaning of the focal length can be found from the equation: an object at infinity has an image at the focal point; an object at the focal point has an image at infinity. "At infinity" means that the light rays are parallel, or collimated.

If the optical system includes an aperture of any sort, it may be necessary to consider the cone of light from the aperture. This can be expressed by the f-number of the system, which is just the ratio of the focal length of the lens f to the diameter of the aperture D. The f-number f/D is frequently written "f */f-number* ".

5.7 Czerny-Turner Spectrometers

Although the basic design dates from 1930, the Czerny-Turner (CZ) monochromator is the most commonly used type of spectrometer today. The design is simple: light enters the instrument through an entrance slit at the focal point of a spherical mirror, so that it is collimated after reflection. The collimated light then reflects from a diffraction grating to a second spherical mirror. The exit slit is at the focal point of the second mirror so that the light gets re-focused to a point on the slit (Figure 5.7).

The CZ spectrometer is a monochromator in that it projects an image of the entrance slit onto the exit plane, and the wavelength band falling over the exit slit is controlled by rotating the diffraction grating. The CZ design has the practical benefit over other spectrometer designs of eliminating coma, an optical aberration turns an image into an overlapping series of circles.

The IDS spectrometer is a CZ-type of focal length 1.33 m and $f/9.4$. The f-number dictates the characteristics of an external entrance optics system, as it is important to force the light to fill, but not overfill, the entrance cone of the spectrometer. If the entrance cone is not full, the entire surface of the diffraction grating will not be illuminated and the resolution of the spectrum will suffer. If the entrance cone is overfull, there will be light that does not get reflected from the first mirror onto the grating. Conceivably, this light might end up incident on the exit plane, distorting the final spectrum.

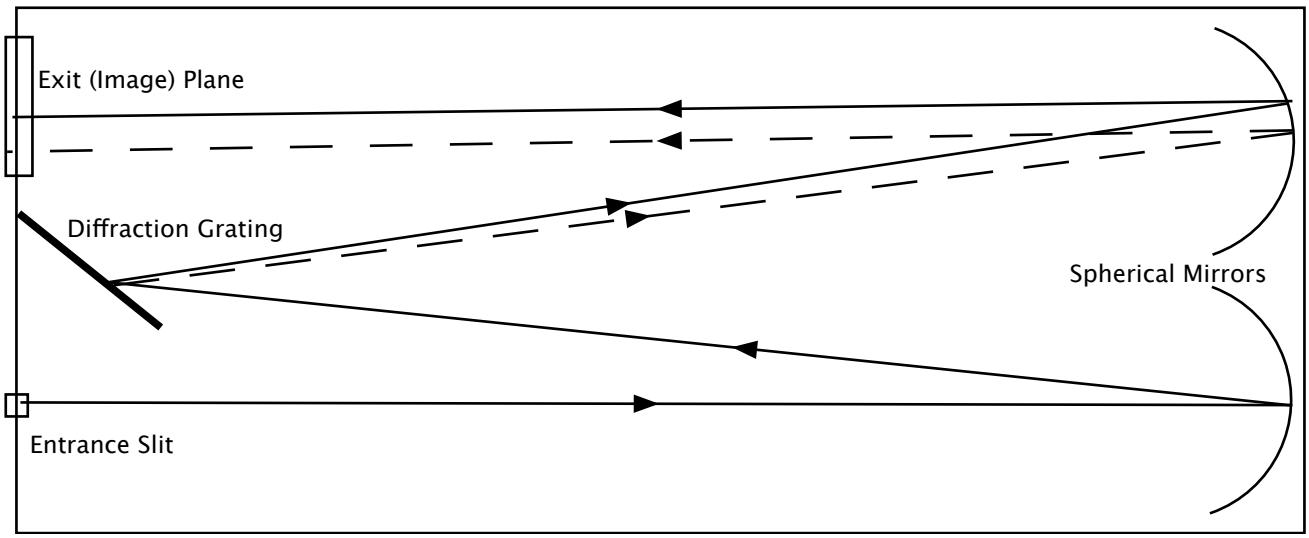

Figure 5.7: Schematic of a CZ-type spectrometer showing the divergence of a bichromatic ray.

5.8 Doppler Shift and Thermal Broadening

Light of frequency ν_0 emitted by a source moving with velocity v relative to an observer is measured to have frequency ν, where

$$\triangle\nu = \nu - \nu_0 = \nu_0 \frac{v}{c} \tag{5.17}$$

This change in apparent frequency is called the Doppler shift. However, since the output of a spectrometer is a measurement of light intensity with varying wavelength, the IDS system measures the Doppler shift of the ions' light by determining the wavelength difference between the observed emission peak and the normal, 'rest', location of the peak. So equivalently, and more usefully for our purposes, the Doppler shift can be expressed in terms of wavelength as

$$\triangle\lambda = \lambda - \lambda_0 = \lambda_0 \frac{v}{c} \tag{5.18}$$

Equations 5.17 and 5.18 are the non-relativistic form of the Doppler shift for sources with velocities well under the speed of light. Since we do not expect the flows in SSX to have velocities of more than several tens of km/s [12], this convenient approximation will be accurate.

The thermal broadening of the spectral lines is due in part to the Doppler shift; in fact, it is frequently referred to as Doppler broadening. Physically, the meaning of the Doppler shift in the thermal line broadening comes from the fact that temperature is proportional to the average kinetic energy of a population. Due to random thermal

motion there is a Maxwellian velocity distribution; there are ions moving in all directions relative to the observer. The greater the kinetic energy, the greater their RMS velocity and so the greater their Doppler shift. The different observed values of the ions' emission wavelengths will therefore distribute around the emission line's central wavelength. Along the direction parallel to v, the distribution function is [32]

$$f(v) = \sqrt{\frac{m}{2\pi RT}} e^{--\frac{m}{2RT}v^2} \tag{5.19}$$

where m is the atomic weight.

We can substitute the frequency distribution due to the Doppler shift $c\triangle\lambda/\lambda_0$ in for the velocity v and so find the full-width half maximum, the distance between points on the distribution whose magnitude is half of the peak [1].

$$\triangle\lambda_{FWHM} = \frac{2\lambda_0}{c}\sqrt{\frac{2RT\ln 2}{m}} \tag{5.20}$$

Since we will be dealing with data rather than with a defined shape, a more convenient measure of width is the standard deviation σ. It is easily determined that for a Gaussian, the FWHM$= 2.36 \times \sigma$.

Hence, we can extract the temperature of an ion population from the width of its lines, assuming that the lines are single Gaussian emission lines. If the width of a peak are is due to overlap from two closely-spaced emission lines, then the relationship of Equation 5.20 is no longer valid and its use would lead to an erroneously high temperature.

Previous experiments on SSX allow us to estimate the width and shift of the spectral line in question. Given an ion temperature of approximately 20 eV [7], or approximately 232,000 K, and a flow velocity on the order of 65 km/s, the wavelength shift of the peak will be approximately 0.05 nm, and the thermal width will be on the order of 0.023 nm. Compared to the spectrometer's dispersion of 0.032 nm/mm and the detector's pitch size of 1mm per pixel, the emission line at 229.7nm should be less than a full pixel in width and should be shifted from its rest location by nearly two pixels. Currently, without any optical magnification of the spectrum, the IDS system cannot resolve a peak smaller than 200 eV. Hence the line during the FRC's steady-state period should not be resolvable. However, an exit optics system is planned that should magnify the image four times, filling up the entire array of 32 PMT's.

6 Calibration

Before examining light emitted by a hot dynamic plasma, it is necessary to examine the response of the PMT array to a line from a cold, quiet source at a known wavelength. This was done using a hollow-cathode lamp coated with cadmium. A cadmium lamp was chosen because cadmium emits strongly at 228.80 nm, less than a nanometer from the chosen CIII line at 229.7 nm.

The calibration consisted of determining the number of photons per second incident on each element in the PMT array. Since the output of the lamp was constant over time, this was equivalent to determining the shape of the cadmium's emission line. This was done by setting an oscilloscope to trigger every time the voltage from the PMT in question went below -10 mV, that is, every time a PMT recorded an incident photon. However, while the triggering system in the oscilloscope was certainly capable of recording the number of counts, the data acquisition circuitry was much slower. Since a large flux of photons was expected, directly counting and acquiring all the triggers was impossible because during the oscilloscope downtime that happened when the triggering system was activating the acquisition system, there would be pulses that the oscilloscope would miss. Therefore, the oscilloscope was set with a holdoff, a number of triggers that it would have to count before data was acquired. Since the counting part of the trigger circuit would run regardless, the only precaution that was needed was to make sure that the time it took the oscilloscope to count the holdoff number of pulses was greater than the time it took the oscilloscope to acquire data. A ramp, a sawtooth signal of frequency 0.5 Hz varying from 0 to 1 V, was sent into the oscilloscope to provide a data signal. This meant that the oscilloscope would measure the voltage of the ramp every time the holdoff number of pulses was counted by the triggering circuitry. Since the variation of the ramp's voltage with time was set to vary linearly from 0 to 1 V every 2 seconds, the voltage difference between the ramp readings gave the time between data acquisitions, or the time it took for the oscilloscope to record the holdoff number of pulses (Figure 6.2). This is the way the count rate for each PMT in the array was found.

Since the measurement was made at 25th order, the free spectral range was small and so the possibility of light from other orders contaminating the signal was present. A filter was therefore put in front of the spectrometer entrance slit to eliminate light of undesired wavelengths. The filter had a Gaussian transmission profile, with peak transmission of 19% at 229.35 nm and a 9.49 nm bandwidth between half-maxima. Therefore the transmission at 228.8 nm, the wavelength of the cadmium lamp, was approximately 18.5%.

With the filter in, the average single pulse shape is shown in Figure 6.1. With a 0.5 Hz ramp signal and a holdoff of 50,000 events, the pulses from PMT 4 triggered the ramp as in Figure 6.2.

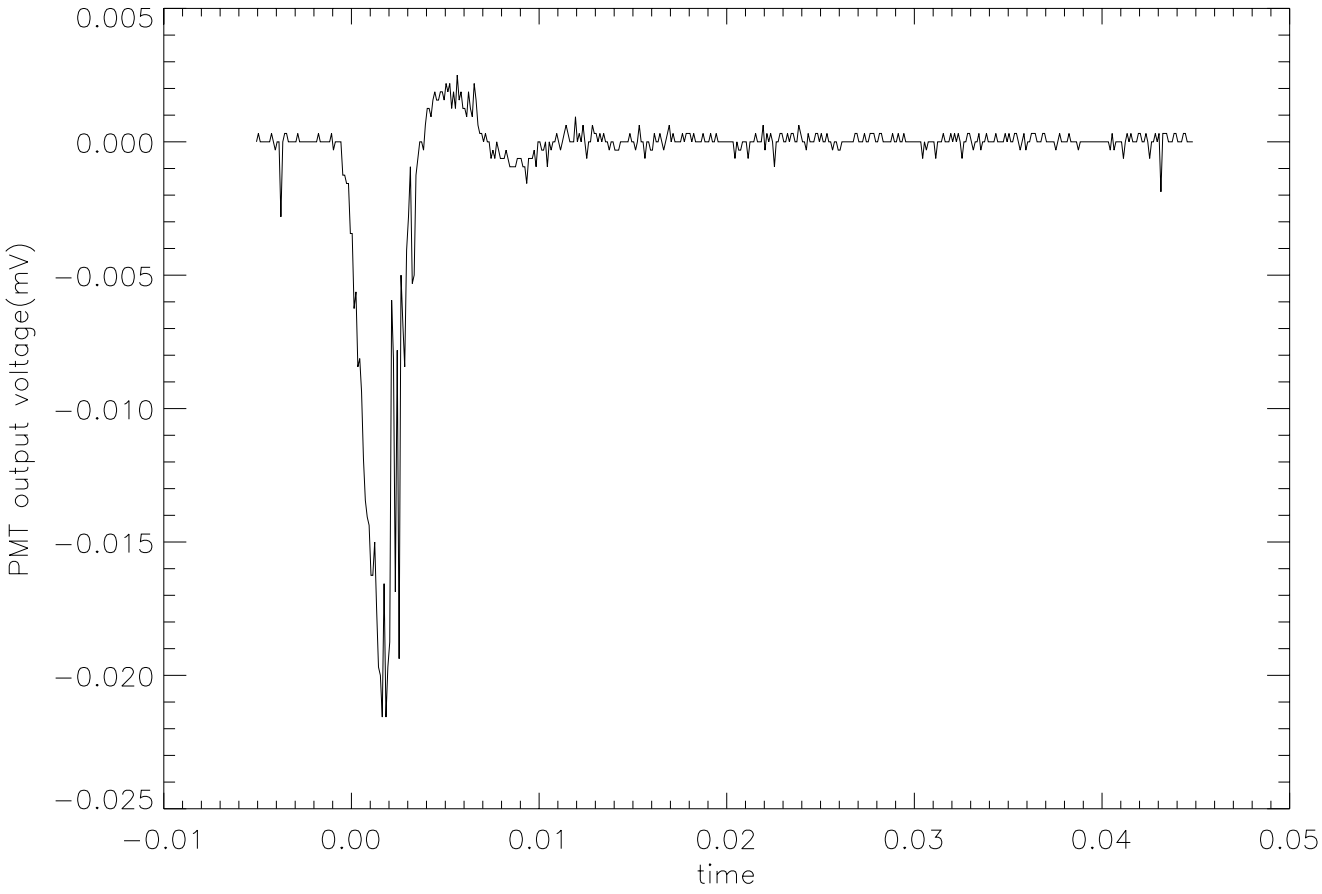

Figure 6.1: Output voltage for PMT 4, the PMT that got the most signal from the lamp.

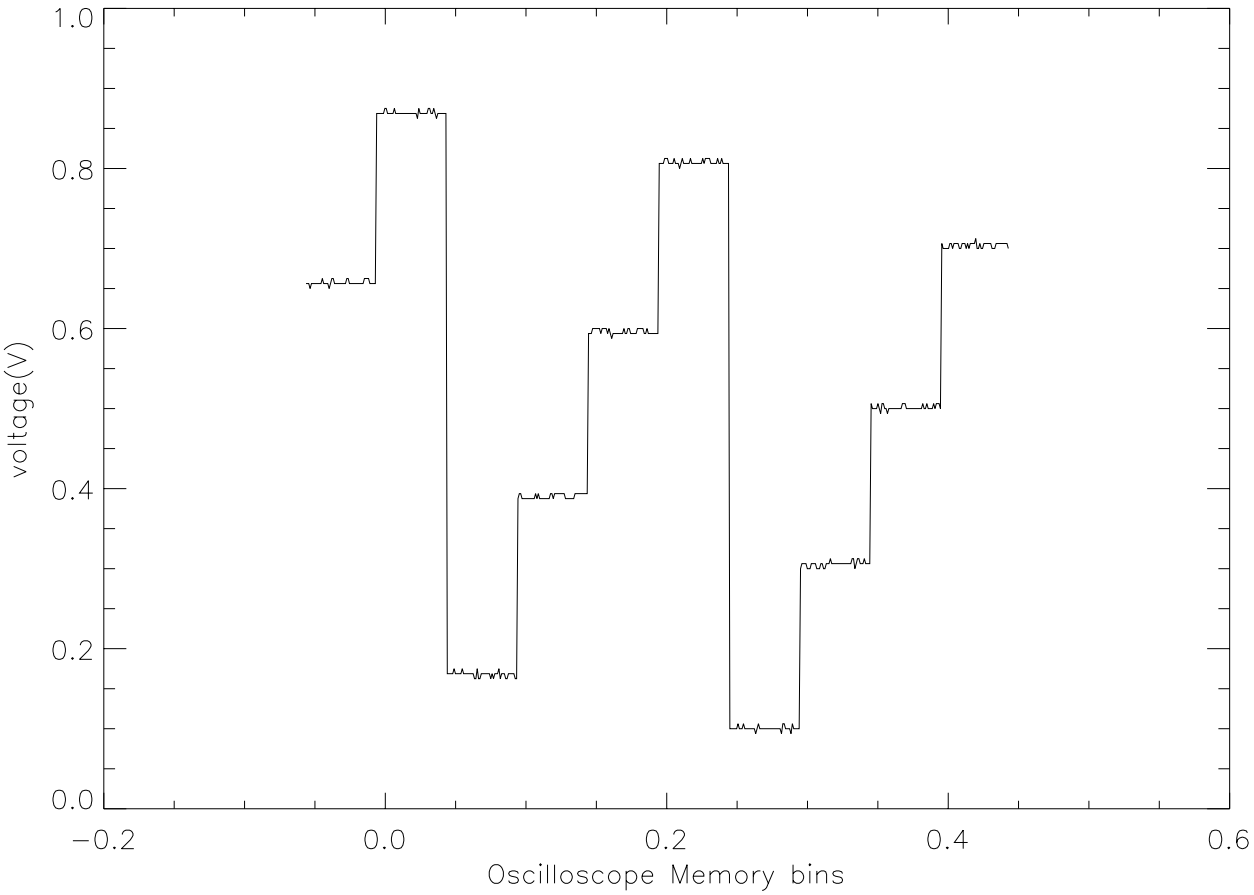

Figure 6.2: 0.5 Hz ramp being acquired every time the oscilloscope counts 50,000 pulses.

Figure 6.2 shows an average difference of 0.215 volts between triggers, not counting the large negative differences incurred when the ramp goes from one cycle to the next. Since the ramp rate is 0.5 Hz, this means that the difference would be 1 volt every 2 seconds. Therefore, the time between triggers for a 0.215 V difference is $\triangle V \times 2s/1V = (0.215 \times 2) = 0.429s$. This time is the amount of time it takes for the oscilloscope to register 50,000 triggers. Hence the count rate is equal to holdoff/time, or $5 \times 10^4/0.429 = 116518$ Hz. Figure 6.3 shows a comparison of count rate for all eight PMT's in the array by PMT number.

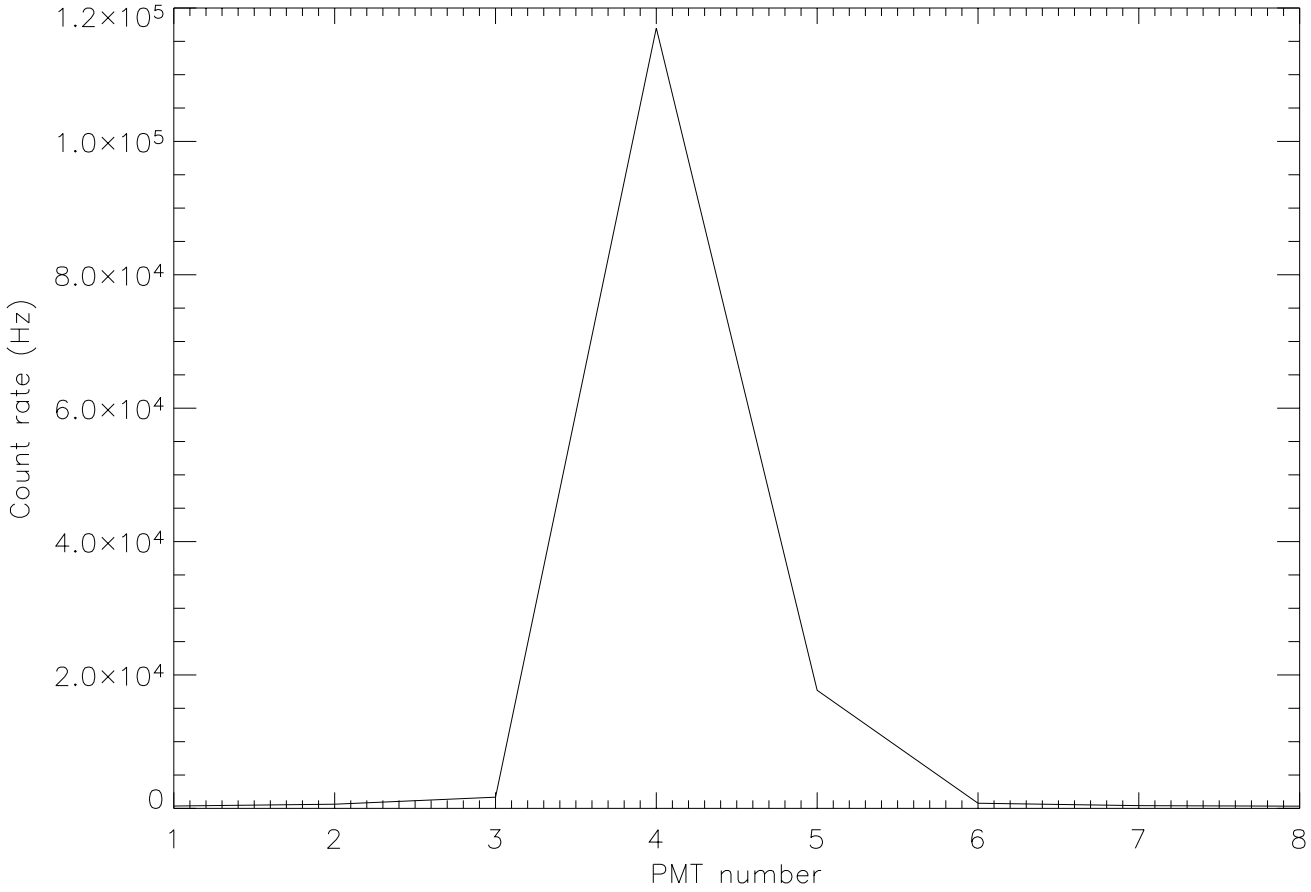

Figure 6.3: The count rate, and hence the signal, across the PMT array.

Figure 6.4 compares data when the filter is in (dashed, same as Figure 6.3), with data without the filter. The unfiltered data has been scaled down by a factor of 16 to equalize the peaks. The factor of 16 means that when the filter is out, PMT 4 gets 16 times the light it gets when the filter is in place. Since the transmission of the filter at the cadmium emission line's wavelength is about 18.5%, we would expect that the PMT would get approximately 5 times the signal when the filter is out. The

fact the it gets 16 times the signal means that when the filter is out PMT 4 gets approximately two-thirds of its light from wavelengths that are not 228.8 nm. This means that there must be a lot of light from other orders hitting the PMT. It is not surprising to find other emission lines besides the stated one at 228.8 nm; the lamp has is a hollow-cathode lamp with a cadmium coating on the cathode, which emits at 228.8 nm when the lamp heats up. However, the cadmium also emits at other wavelengths besides, and it is also highly likely that there are significant impurities in the coating that have their own characteristic emission lines. The presence of all of these other emission lines that hit PMT 4 at certain orders are what cause the extra signal. These other lines are also responsible for the count rate on PMT 3, which is virtually dark when the filter is in.

Clearly, the cold line is mainly confined to a single array element. There is, however, some light on PMT 5—about 15% of the peak. For such a high percentage, it cannot be crosstalk between PMT's alone, since the array is rated at 3% crosstalk. However, it is not so high that it would indicate that the peak straddles the two pixels to any degree. Therefore it seems probable that the cold line is not wider than a single pixel. Since a width less than a single element is to be expected given that the lamp is certainly not hotter than 200 eV, it indicates that the array is well-positioned with respect to the exit plane, that the image of the line is not so blurred as to cause significant widening.

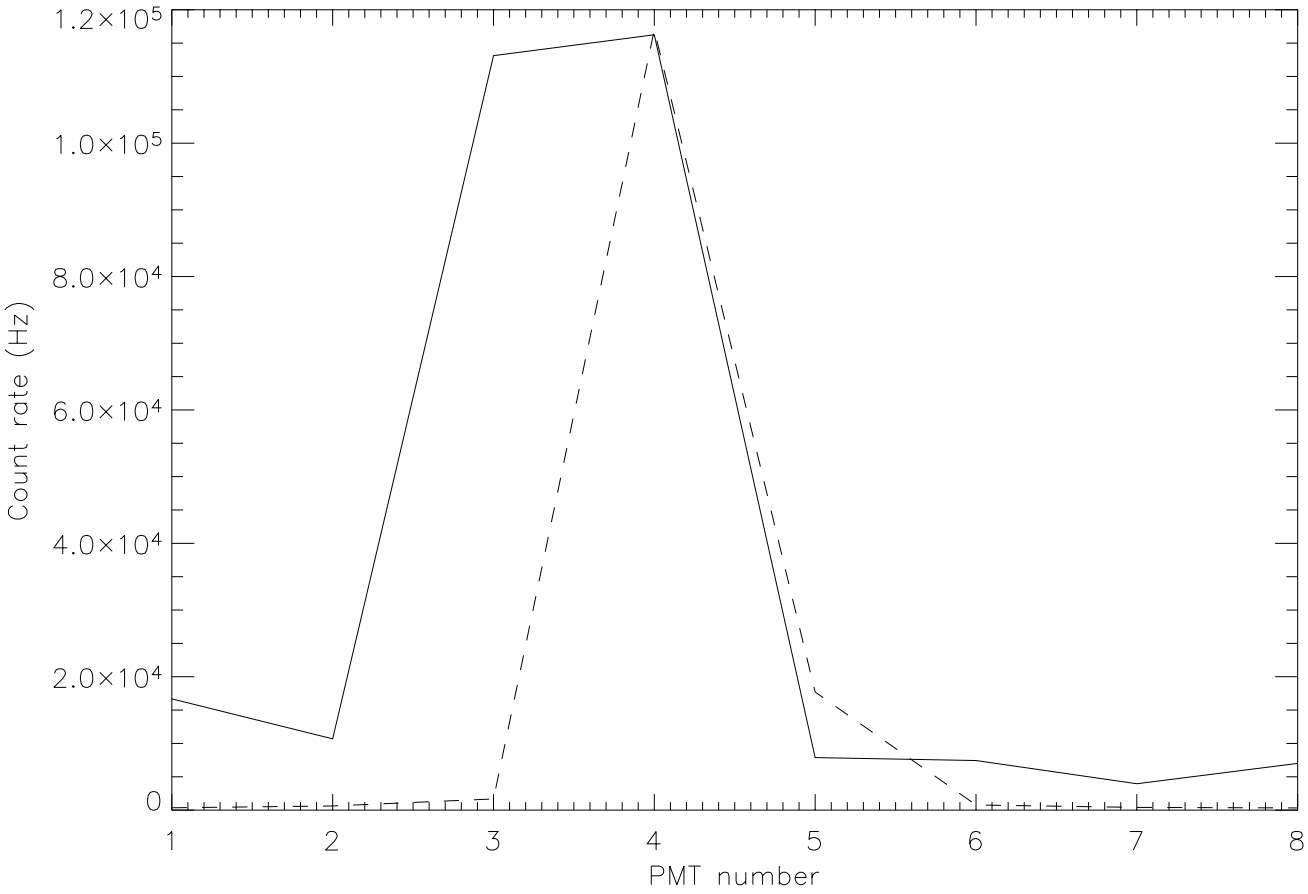

Figure 6.4: Filtered (dashed) versus unfiltered data.

7 Experimental Data

7.1 PMT Saturation

A total of twenty data runs were done, for varying PMT voltage and entrance slit width. When deciding which of these runs to take as accurate representations of the light coming from SSX, it was necessary to compare the PMT array response to the ideal response. The problem is as follows: When photons strike the photocathode in a PMT, photoelectrons are emitted. This photocurrent, initially perhaps only 1 electron per 10 incident photons, is amplified by a series of secondary emitters, called dynodes (Figure 7.1). These dynodes, 10 in each PMT in SSX's array, are kept at a given voltage by a voltage divider so as to amplify the incident photocurrent by a factor of approximately 10 [11] per PMT.

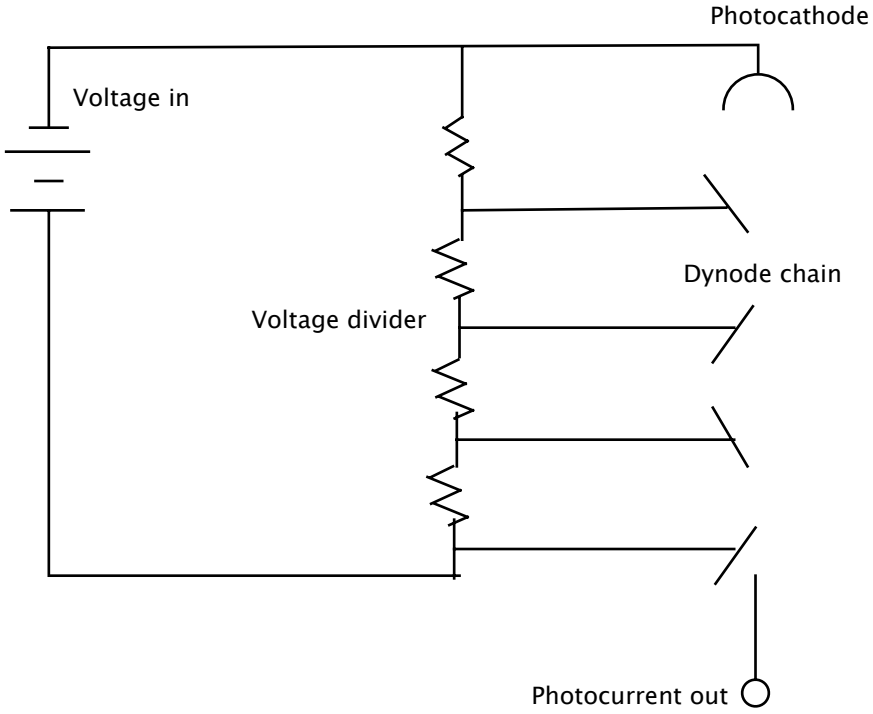

Figure 7.1: A schematic diagram of a photomultipler tube with 4 dynodes.

The correct operation of the PMT relies on the current coming from each dynode not being large enough to disrupt the voltage of the dynode. If the current become too large, the dynode will draw too much power from the voltage divider and the dynodes further down the chain will suffer a drop in voltage. If this happens, the output of the final dynode will not, in general, scale linearly with the initial photocurrent and hence will not accurately reflect the magnitude of the photon flux. A PMT

is said to be *saturated* when this non-ideal behavior occurs. The photocurrent can become too large due to two factors: (1) the initial photon flux is large, causing a big photocurrent from the outset that gains to the point of saturation, or (2) the voltage on each dynode is too large, thus emitting a too-high number of electrons at each step, eventually leading to saturation further down the chain. To ensure that the initial flux is not too large, the entrance slit width must be controlled. To ensure that the voltage on each dynode is not too large, the PMT voltage must be kept low.

An IDL code was used to visualize the data (Section 11). Figure 7.2 shows the traces from each PMT in the array for a run where the PMT's were set at 600 V and the slit was 0.5 mm wide. The code averaged the trace data, taking the average of each 100 points. The total PMT signal for each run was found by integrating the averaged data for PMT 4 from 45 μs to 70 μs. The signal variation with slit width was plotted in Figure 7.3. The signal variation with PMT voltage when the slit width was 1/2 mm was plotted in Figure 7.4 and the signal variation with voltage when the width was 1/8 mm was plotted in Figure 7.5.

PMT 4 was chosen because in all the runs it received by far the most signal. It was felt that comparing the signals from just PMT 4 for all the runs would give a valid estimate of how the signal changed with PMT voltage and sit width, as opposed to averaging the signals from all PMTs in the array. The signal integration was done from 45 μs to 70 μs because we know the qualitative behavior of the plasma between those times. At 45μs the spheromaks should be reaching the midplane and beginning to reconnect, and at 70μs the FRC should be formed and in its steady-state configuration. Including prior and subsequent times in the integration risked including times when either the signal might not be due to the plasma but due to some part of the spheromak formation or the light from the plasma might be in some way affected by the decay of the FRC, particularly the times between 150–200 μs when the FRC has almost certainly decayed and whatever remains is emitting light in some disorganized manner.

Figure 7.3 shows the variation of output with changing slit width, from 1/8 mm to 3/4 mm, at a constant voltage of 550 V for PMT 4, the PMT with the most signal. For slit width, it makes intuitive sense that the output signal should vary linearly with the slit. Hence we expect output to scale linearly with width when the voltage is not changed. The dashed line in Figure 7.3 is a straight line through the origin, to indicate how we expect the signal to vary of it is not saturated. Although there is a noticeable offset, the output scales linearly with slit width until the PMT saturates by the final point, a width of 0.75 mm. While the root cause of the offset is unknown, it could be caused by one of two things. First of all, all photomultiplier tubes emit some small amount of current even when there are no incident photons. Such a current is called *dark current*. However, the datasheet for the PMT array (model: Hamamatsu H7260) indicates that the maximum dark current, for PMT voltage at the maximum, is 2 nA. This compares to an average current per PMT at the same voltage of 6 μA,

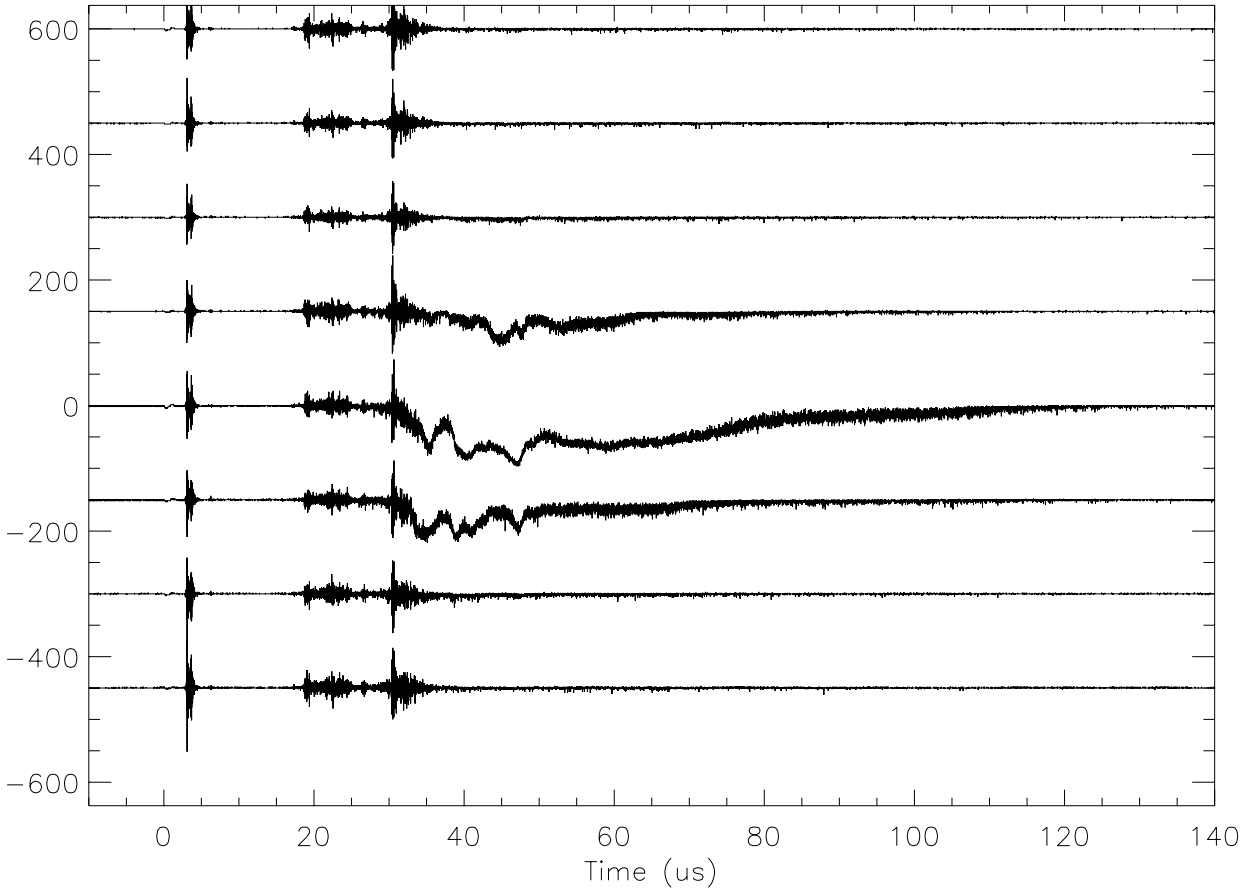

Figure 7.2: Traces of the output of each PMT in the array, voltage=600V, slit width=0.5 mm.

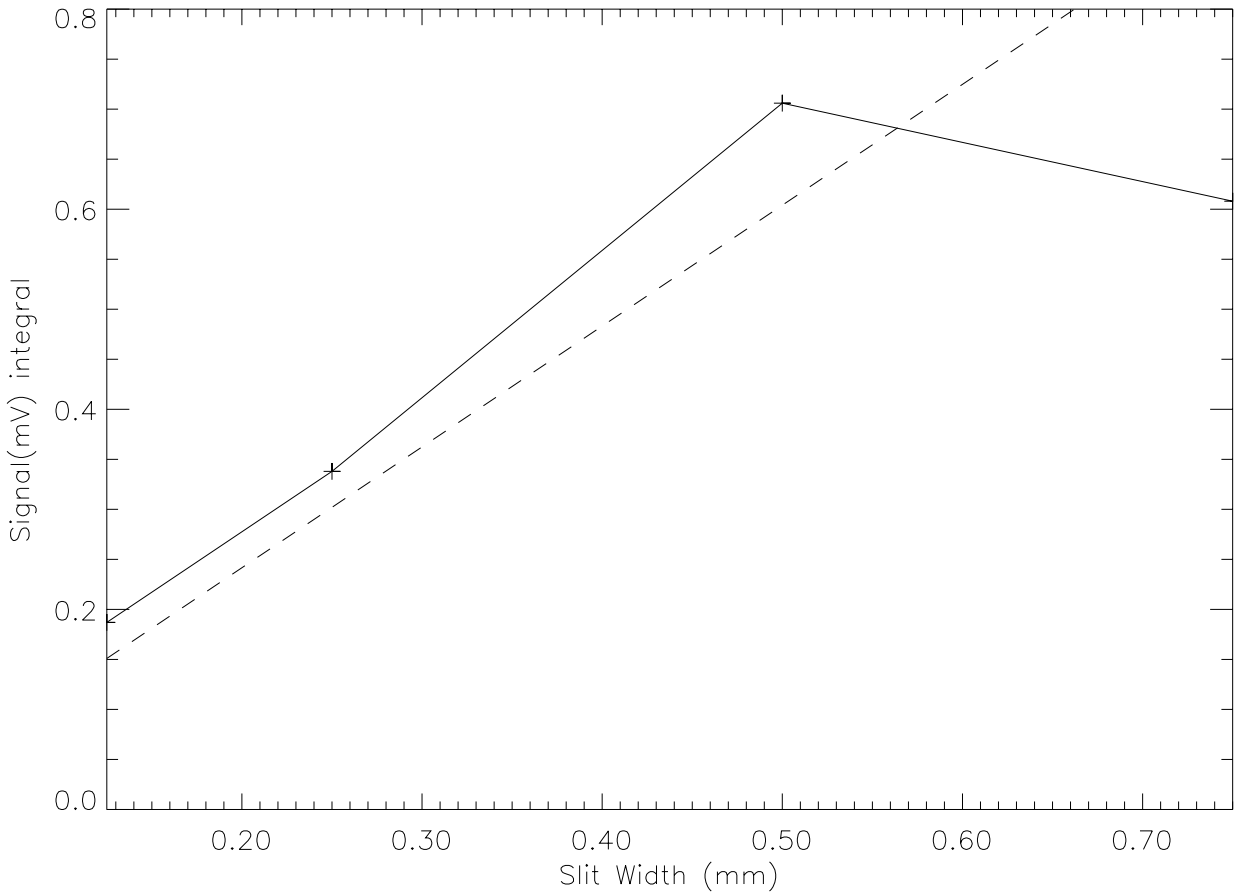

Figure 7.3: Variation in total signal when the slit width is changed at a PMT voltage of 550V (solid) compared to a line passing through the origin, i.e going to zero when the slit is closed.

3000 times greater. Therefore the dark current should not be a significant effect. The other possibility is that the light beam into the spectrometer is non-uniform, causing the signal to vary non-linearly as the slit width changes. In any case, the scaling is of greatest importance, and Figure 7.3 shows that the tube is unsaturated until the slit is at its widest.

Since the datasheet for the array gave a relation between PMT voltage and gain, it was determined that gain scaled as (voltage)^9. Since the sweeps of voltage values did not change slit width and hence did not change the incident photon flux, the output of the PMTs should scale as the ninth power of the voltage. There were two voltage sweeps from 550 V to 750 V in increments of 50 V; one with a slit width of 1/2 mm (Figure 7.4), and the other with a width of 1/8 mm (Figure 7.5). Since we know from Figure 7.3 that neither of these widths is sufficient to saturate the tube at 550 V, it was assumed that the first data point represented unsaturated response and so a ninth-power curve was plotted on both graphs beginning at that initial data point.

In both voltage sweep plots initial ideal scaling followed by rapid saturation can be seen. This indicates that only the 550 V and 600 V runs are certain to be unsaturated. In Figure 7.5, however, the third data point (at 650 V) seems anomalous, especially since it shows a decrease in photocurrent for an increase in PMT voltage. As it is, both voltage sweeps deviate from ideal behavior at the same voltage, irrespective of slit width. One would expect the 1/8 mm sweep to deviate at a higher voltage than the 1/2 mm sweep, since it is getting 1/4 the photon flux at a given voltage. If the anomalous point were at a higher signal, however, then it could be seen that the 1/8 mm sweep actually saturates at a higher PMT voltage than the 1/2 mm sweep, as intuition would suggest. To investigate, consider the 650 V data point on the 1/2 mm sweep. Since the other data indicate that the slit scaling seems to be linear for those widths, we might expect it to be getting 4 times the signal that the anomalous point is getting. In fact, it is getting 5 times the signal. All these factors point towards the 650V, 1/8 mm datum being problematic for some reason.

Based on the saturation plots, the run taken with a PMT voltage of 600 V and slit width of 0.5 mm was chosen for further investigation (traces shown in Figure 7.2). The voltage and width parameters were chosen to be at the known limit of the linear PMT response regime, so as to ensure the maximum light on the array without saturating it.

7.2 Experimental Error

There were two possible sources of error in the measurements: statistical and systematic. The statistical error, equal to $\sqrt{n}$, is expressed as PMT counting errors. Since the PMT's are 8-bit, the error caused by varying the least significant bit is 1/256. The oscilloscopes were set to 20 millivolts per division, making the statistical

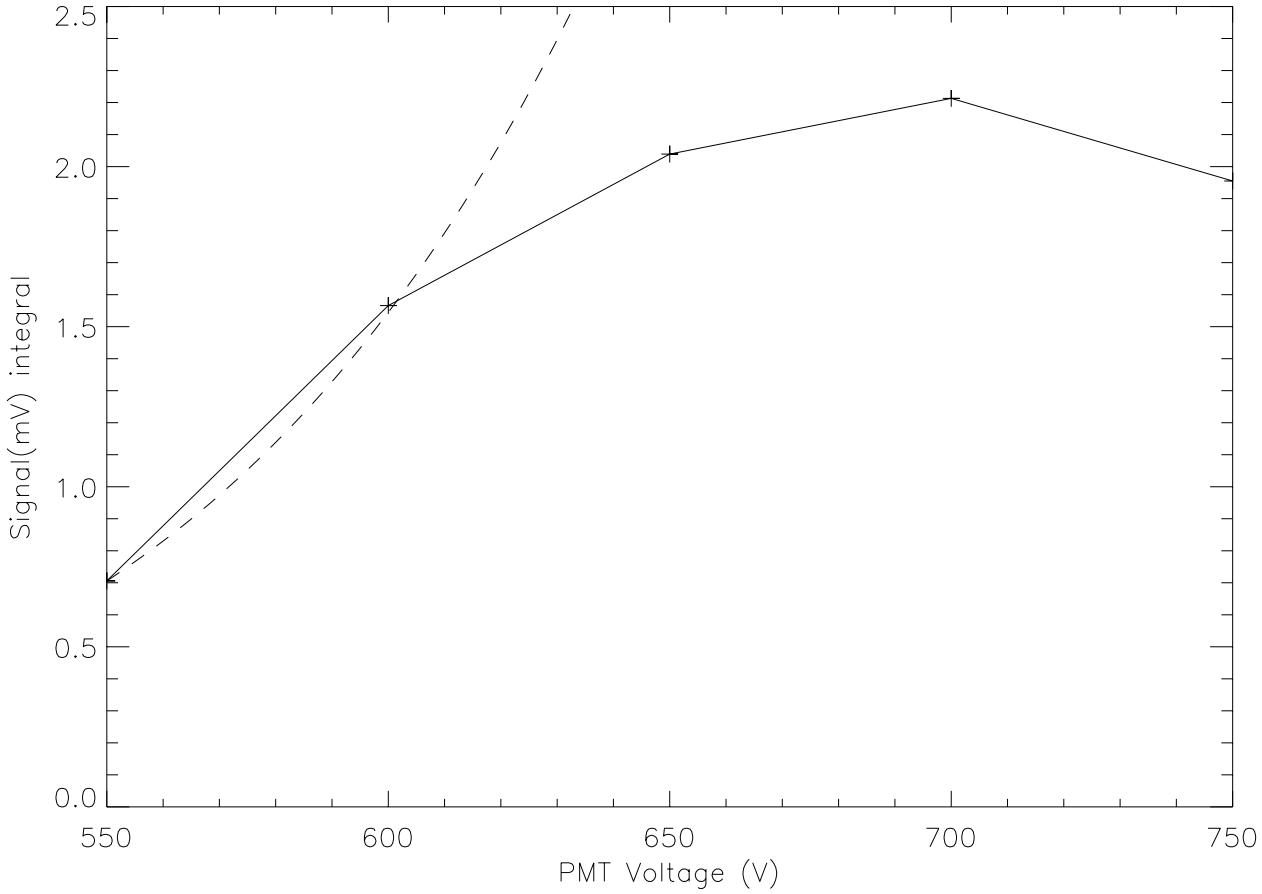

Figure 7.4: Variation of total output signal with PMT voltage for a 1/2 mm slit (solid) compared to a ninth-power function (dashed).

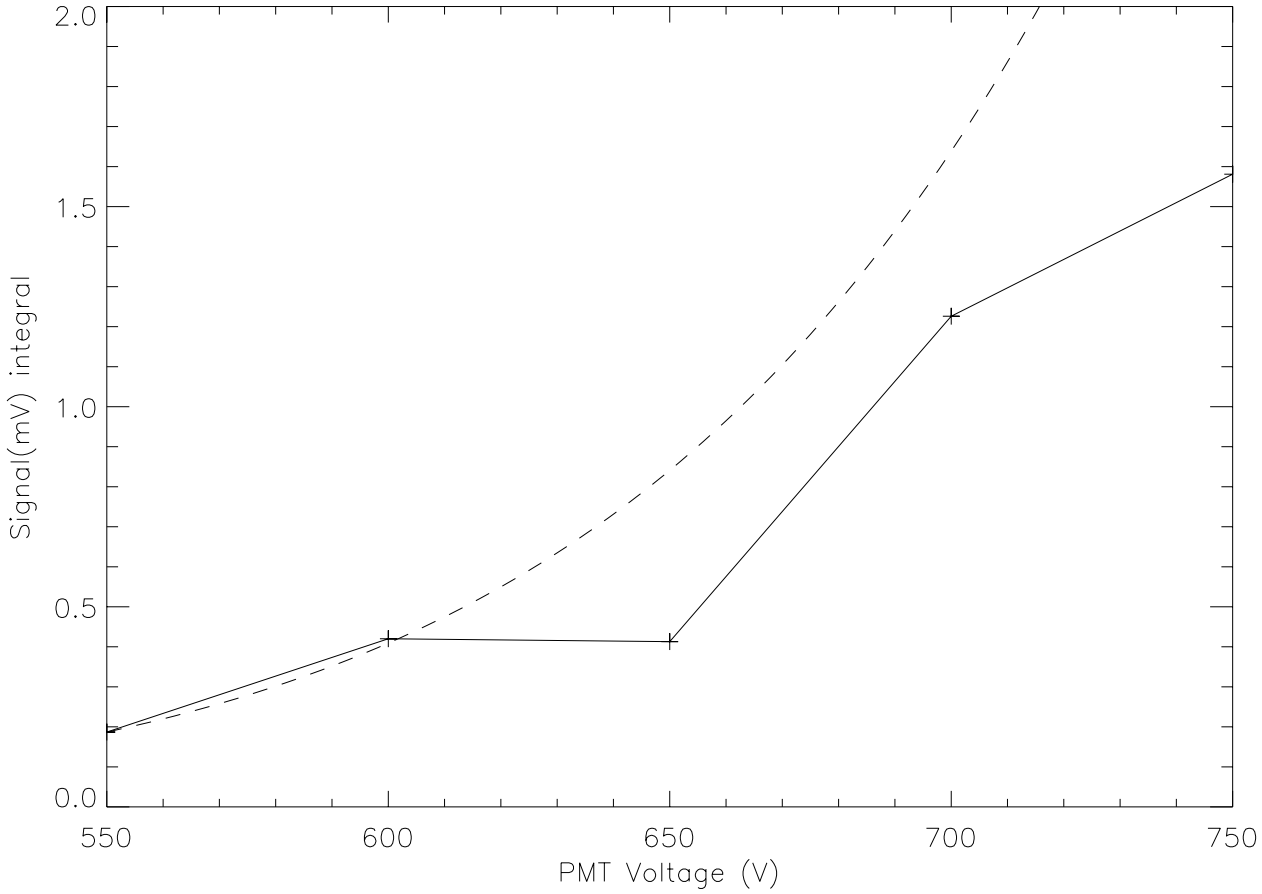

Figure 7.5: Variation of total output signal with PMT voltage for a 1/8 mm slit (solid) compared to a ninth-power function (dashed).

error $(20 \times 8)/256 = 0.625$ mV. Since the channels with signal generally got between 50–100 mV of signal (Figure 7.2, the error on the values that make up the peak were between approximately 1–0.5%. The averaging of every 100 data points also affects the statistical error, reducing it by a factor of $\sqrt{100}$, or 10. Hence the statistical error is tiny and is not taken into account in the data presented here.

There are also sources of systematic error. The first is anode non-uniformity. The relative outputs of the PMT's are not the same, varying by as much as about 8%, according to the PMT array datasheet. The second is cross-talk, the process by which input into one PMT ends up as output from the adjacent PMT's. The datasheet for the array rates the typical average signal from two dark channels adjacent to a bright channel as 3%. The error due to anode non-uniformity is easily eliminated by multiplying the data by some normalizing factor, and the error due to cross-talk is eliminated by deducting 1.5% of a channel's data reading from the data for the adjacent channels (See Section 11 for the factors). This elimination of cross-talk assumes that the signal bleed is relatively isotropic and does have a preferred direction.

Since the statistical error is miniscule and the systematic error has been eliminated as much as possible, the error is not displayed on any of the figures that are based on experimental data.

7.3 Temperature and Velocity Measurements

The shape of the line (Figure 7.6) is found by plotting a constant-time slice of the traces. The velocity (Figure 7.7) is found by line-averaging the traces along the length of the array. This gives the location of the centroid of the line, which is related to the velocity by the Doppler shift formula $\triangle\lambda = \lambda_0 \cdot v/c$. The uncertainty in the velocity, given that the centroid's location within the array element is difficult to measure precisely at this resolution, is given by plotting velocity curves that shift the measured centroid by 1/2 the width of an array element.

Determining the plasma temperature from the lineshapes was done with an addition to the code. In Figure 7.6, the points making up the lines consist of ordered pairs of numbers $(x1, f1), (x2, f2), \ldots, (x8, f8)$ where the x's are the position ordinates and the f's are the magnitudes of the signal. If these numbers are used to construct a set of x's, the multiplicity of each x being its associated f, then this set plotted as a histogram reproduces the line given by the ordered pairs. Statistical measurements done on the histogram data will now give results in coordinate numbers rather than in magnitude numbers.

Under our initial assumption that the line represents a single Gaussian emission line, the width (FWHM) of the line can easily be found from the standard deviation of the

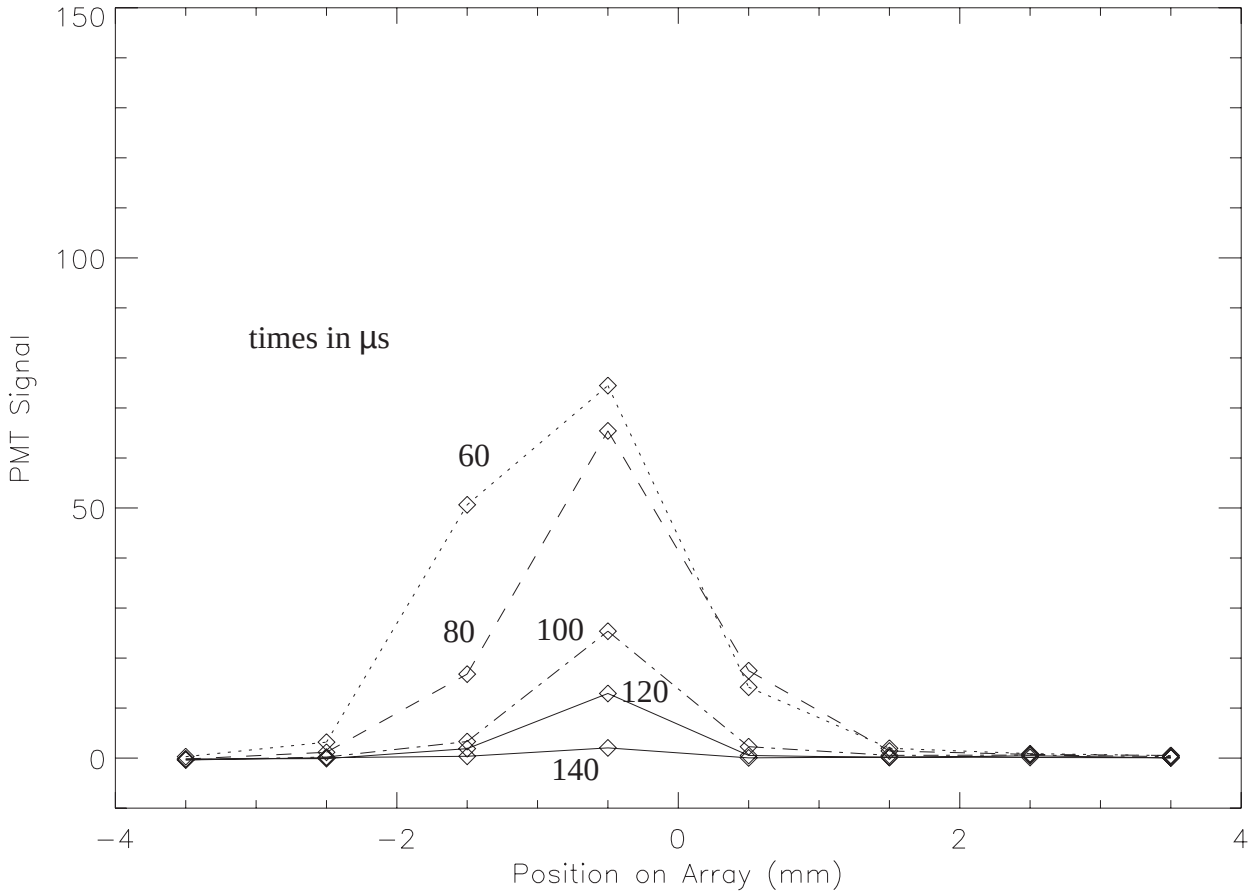

Figure 7.6: Lineshape for 5 different times.

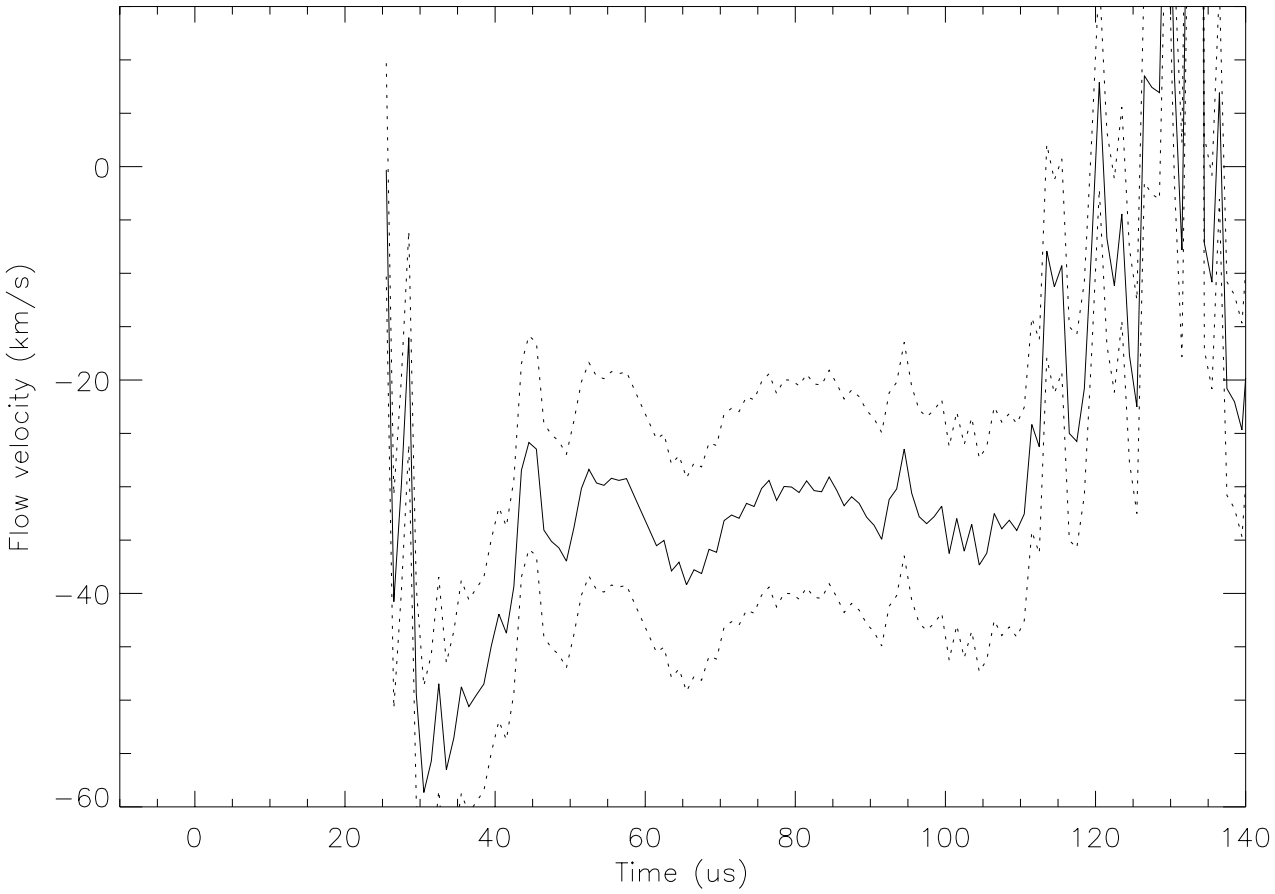

Figure 7.7: Velocity (solid) of the centroid. The dashed lines are the uncertainty given that the centroid could be anywhere within a 1mm ($\triangle\lambda = 0.032$nm) pitch array element.

histogram data since the $FWHM = 2.36 * \sigma$ for a Gaussian distribution. The width is related to temperature by Equation 5.20, so the temperature of the plasma can be plotted as a function of time by finding the linewidth at each time value (Figure 7.8).

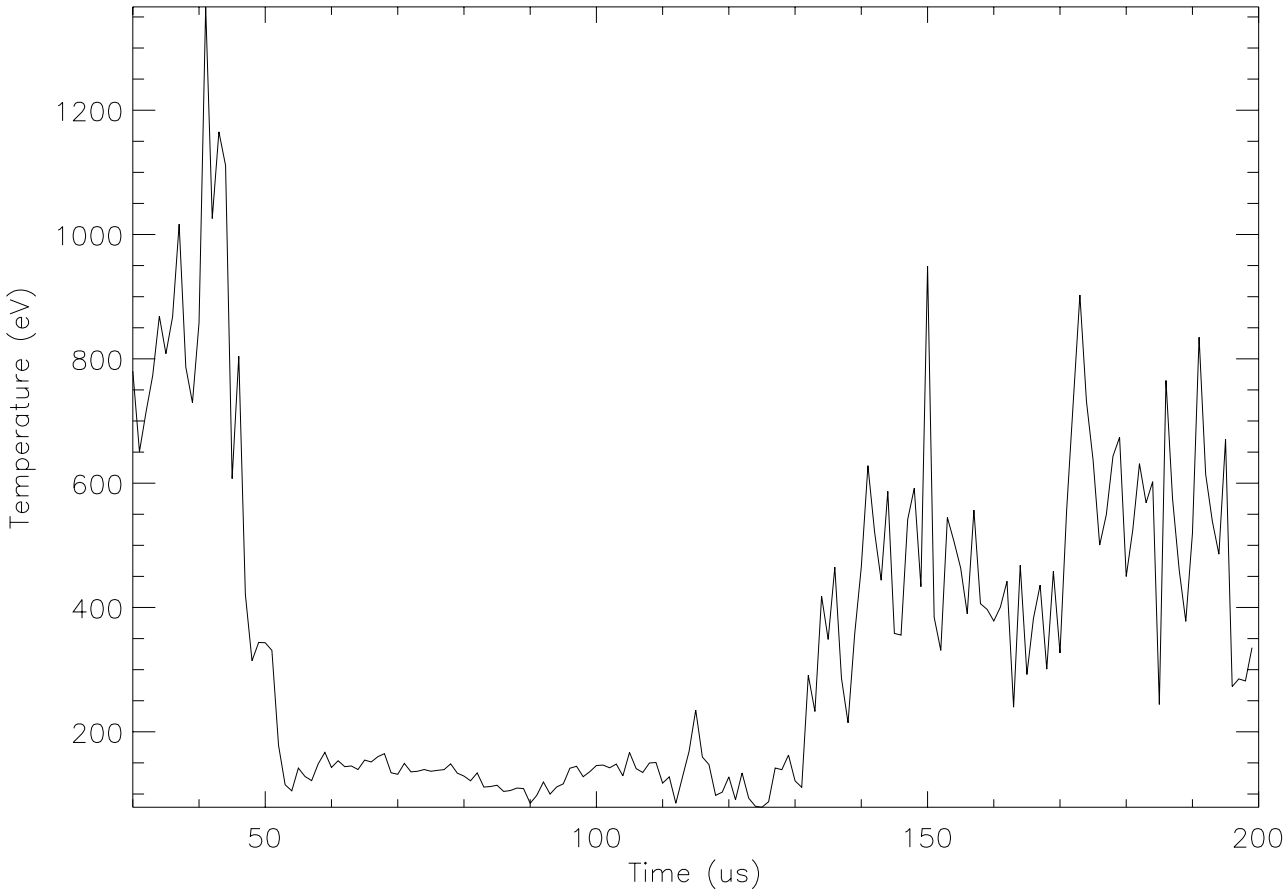

Figure 7.8: Temperature as calculated from the linewidth (assuming a Gaussian shape) for the run after 30μs.

The theory that velocity shear is responsible for the higher-than expected linewidths can most easily explain the sudden sharp drop in linewidth seen around 50 μs (Figure 7.8). If oppositely directed jets are widening the line then those jets, being a product of reconnection, should die down when reconnection is complete, at around 50 μs [13]. Since the time of the drop corresponds to the time by which we expect the FRC to be formed [28] and the linewidth thereafter is at the minimum of resolution, the shear hypothesis gains considerable strength from Figure 7.8.

If we assume that line overlap due to shear is responsible for the linewidth, we can obtain a crude estimate of velocity. Since Section 5.8 tells us that the real line should

be less than a single pixel, or 0.032 nm, in width, we can assume that the "line" we are measuring is made up of two lines whose centroids are 0.032 nm apart. Hence the relative velocity of these lines should be, from Equation 5.18,

$$\mathbf{v} = \frac{\triangle\lambda}{\lambda_0} \times c = \frac{0.032}{227.9} \times (3 \times 10^8 m/s) \sim 4cm/\mu s \tag{7.1}$$

This is approximately half of V_A, the Alfvén speed (the characteristic speed of propagation for a perturbation in a magnetic field line) for SSX-FRC. Assuming that the two lines have equal velocity, their absolute velocity in the lab frame should therefore be approximately $0.25V_A$. Hsu et al [22] found in magnetic reconnection experiments that the outflow from the reconnection region was approximately $0.2V_A$, very close to the crude estimate (Equation 7.1) for SSX's outflow speed should the shear hypothesis be correct. Moreover, an older SSX measurement of velocity by Kornack et al. [23] found Alfvénic speeds, $v = V_A$. At that time SSX was not in the current SSX-FRC configuration and allowed for only partial reconnection along the spheromaks. The velocity from the older SSX configuration should be higher than the velocity attainable by SSX-FRC since the jets emerged from only a few locations and so did not disturb each other and slow one another down. However, the older measurement should be around the same order of magnitude as the more recent one. In other words, especially given the IDS system's low resolution, the current estimate of $\sim 0.25V_A$ is in agreement with experimental values.

While the temperature for the steady-state FRC is not resolvable, it is clearly under 200 eV and so does not deviate from expectation.

8 Analytical Model

Since an IDS diagnostic necessarily measures an average temperature and flow velocity along its chord, it seems clear that the less homogenous and more dynamical a plasma, the less meaning the raw IDS output should have by itself. Consider an IDS diagnostic of a plasma with oppositely directed jets. It makes intuitive sense that oppositely directed jets resulting from a shear in the plasma flows should cancel one another out to some extent in the IDS data resulting in a final peak location that is an average of the two. However, since the emission lines have finite width, one can think of the process of cancellation as being more like merging of lineshapes. One can imagine two close lines of equal magnitude merging together to make a single line whose centroid is the average of the initial two lines', but whose width is the extent of the two close lines (Figure 8.1).

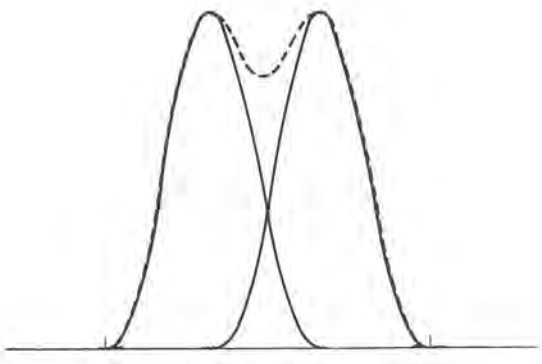

Figure 8.1: The real (solid) Gaussians overlapping to form the (dashed) wider image.

As previously discussed, SSX plasmas are highly dynamical and indications are that such a velocity shear might be taking place. Certainly, the linewidths are much larger than expected. Therefore, the following simple analytical model aims to examine the IDS output for various flow profiles and make the preceding discussion of lineshape and centroid location more quantitative.

Consider the following ideal representation of SSX (Figure 8.2): A cylinder containing purely azimuthal flows with no axial variation. A circular slice of the plasma therefore suffices:

The radial vector to the chord is at an angle θ to the diameter, and the chord is at an angle ϕ to the diameter. A closer look at the geometry of the chord in relation to the radial origin (Figure 8.3) will let us set up the problem. The desired result is an expression for the flow magnitude along the chord at a point along the chord, $\mathbf{v} \cdot d\mathbf{s}$.

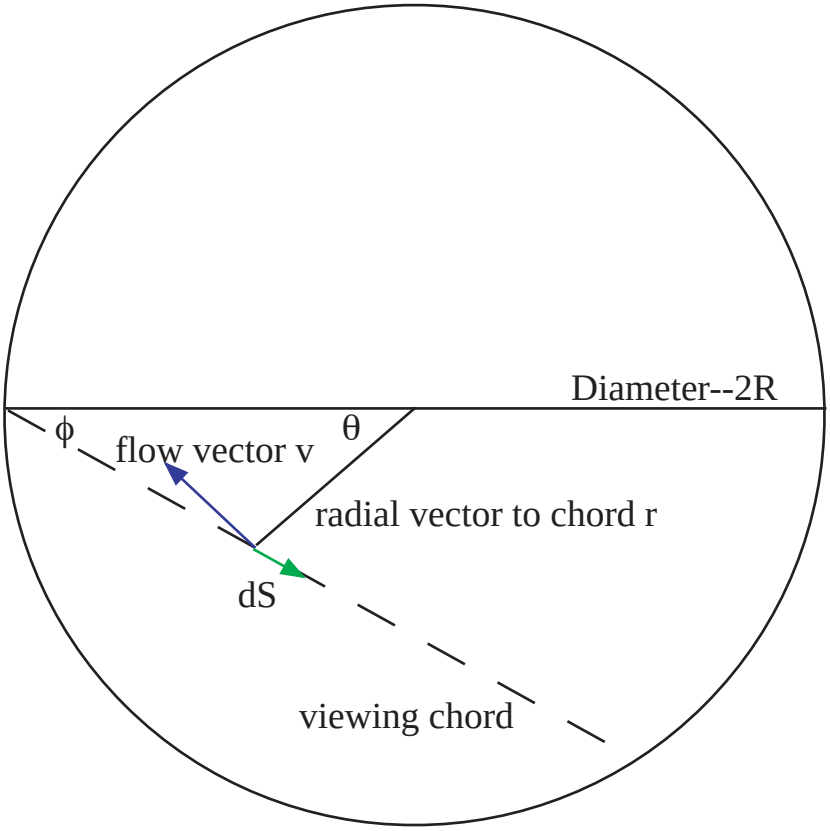

Figure 8.2: A simple drawing of a slice of SSX with viewing chord and flow vector.

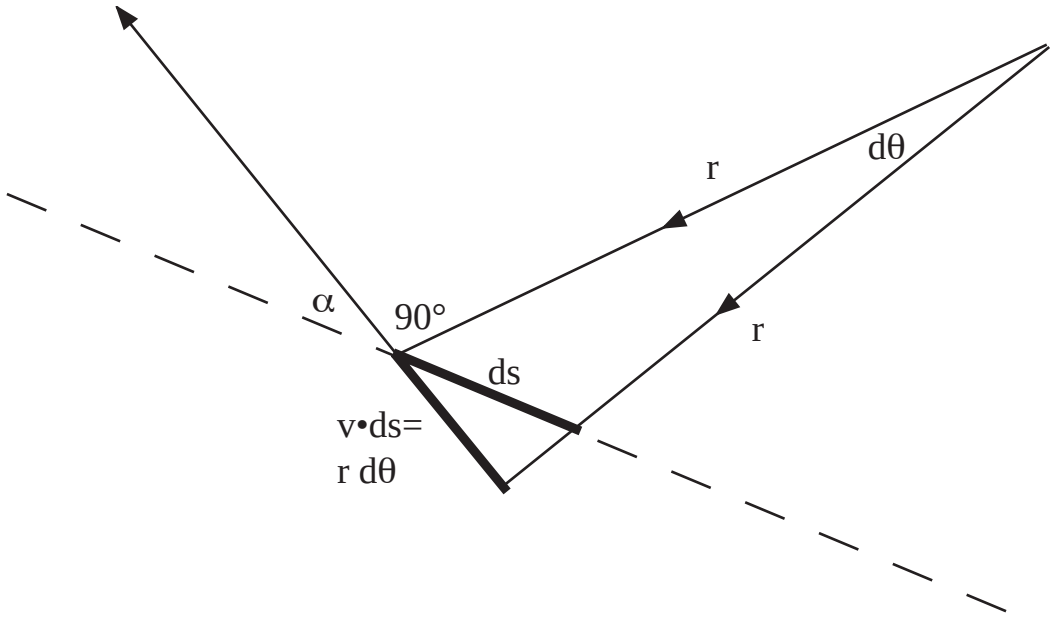

Figure 8.3: Geometry near the viewing chord.

$\mathbf{v} \cdot d\mathbf{s}$ can be thought of as the magnitude of $\mathbf{v}$, $\mid \mathbf{v} \mid$, times the projection of $d\mathbf{s}$ along $\mathbf{v}$. From Figure 8.3, it is clear that

$$(d\mathbf{s} \text{ along } \mathbf{v}) = r d\theta \tag{8.1}$$

where from Figure 8.2,

$$r = \frac{R \sin\phi}{\sin(\phi + \theta)}, 0 \leq \theta \leq \ 180^\circ - 2\phi. \tag{8.2}$$

Let us use this to investigate the lineshapes that result from different flow profiles $\mid \mathbf{V} \mid$.

8.1 Linear Flow Profile

The most simple (nonzero) flow profile is of a fluid rotating like a rigid rotor, with $v = \omega r$. In a fluid with this profile, the velocity would increase linearly with radius, reaching a maximum at whatever boundary we put on the fluid. The rigid rotor is hence not a physically valid representation since it makes the fluid's parameters independent of the container. Nonetheless, it is an easy first profile to use to demonstrate the analytical model developed here.

Since we expect the velocity to peak at approximately 65 km/s, a possible linear flow profile would be

$$\mid \mathbf{v} \mid = 65 \frac{r}{R_0} km/s \tag{8.3}$$

going from 0 km/s in the vessel's centre to 65 km/s at the outer edge where $r = R_0$. Hence we have an IDS signal from each element of the chord

$$\mathbf{v} \cdot d\mathbf{s} = \frac{65}{R_0} r^2 d\theta \tag{8.4}$$

Taking R_0 to be unity and plotting the signal for different values of chord angle ϕ, we get Figure 8.4.

We can determine the shape of the emission line at 227.9 nm that a hot plasma would have were it to rotate like a rigid rotor by replotting the information in Figure 8.4 as a histogram (Figures 8.5 and 8.6). This bins chord element signals that are close to one another together, resulting in a lineshape. This should show the distribution of velocities that make up a given signal and hence give a quantitative idea of the lineshape and width due to the velocity shear. We can see from Figures 8.5 and 8.6 that while the lines have some spread out from the main peak, none of the chord angles for a linear flow profile result in a double-peaked distribution. The velocities of the signals have been converted to wavelength shifts.

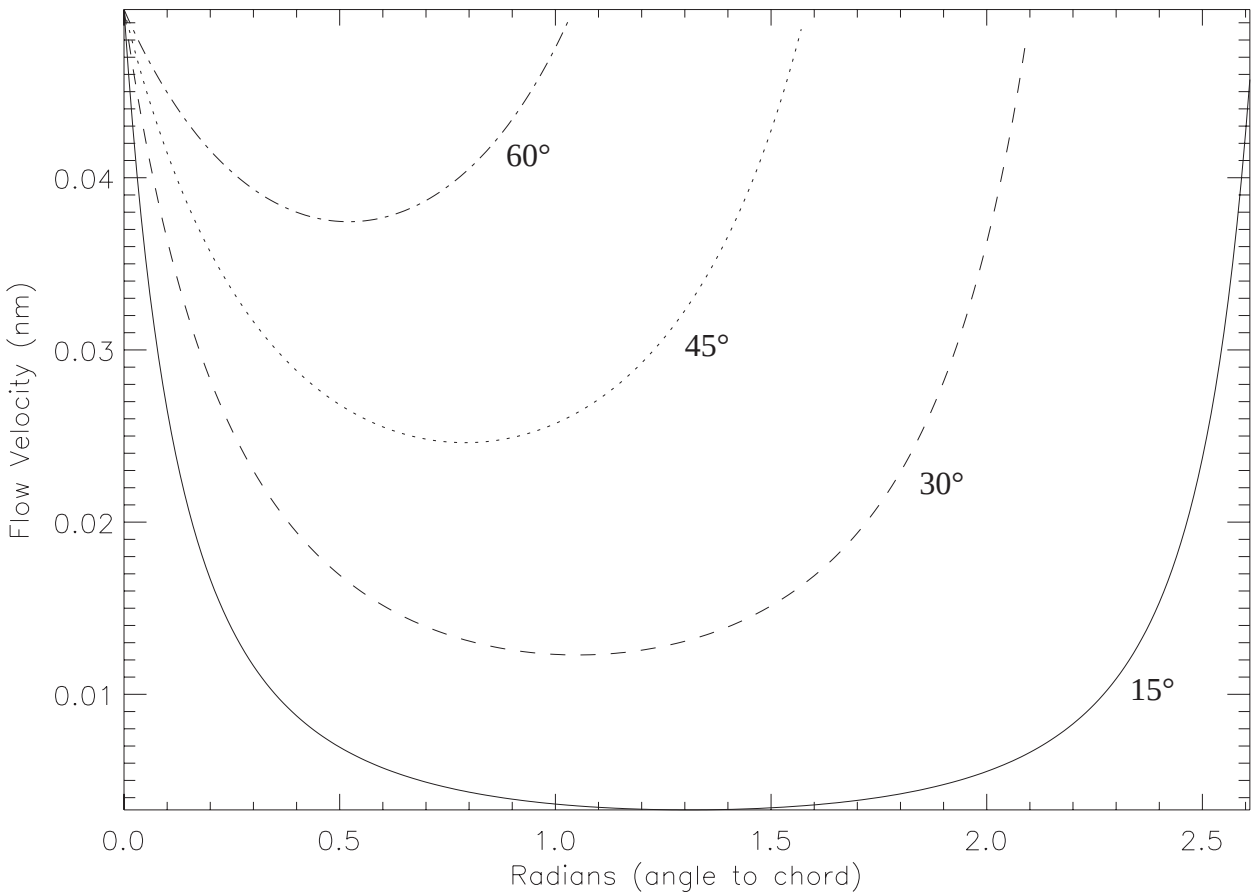

Figure 8.4: Signal obtained by an IDS system from each chord element for four different chord angles ϕ from a fluid with a linear flow profile.

Figure 8.4 is easy to interpret. The smaller the chord angle ϕ, the longer the chord has to be (Figure 8.2. Hence the different numbers of points for the chords. Also, the longer the chord, the more velocity variation the IDS system will "see".

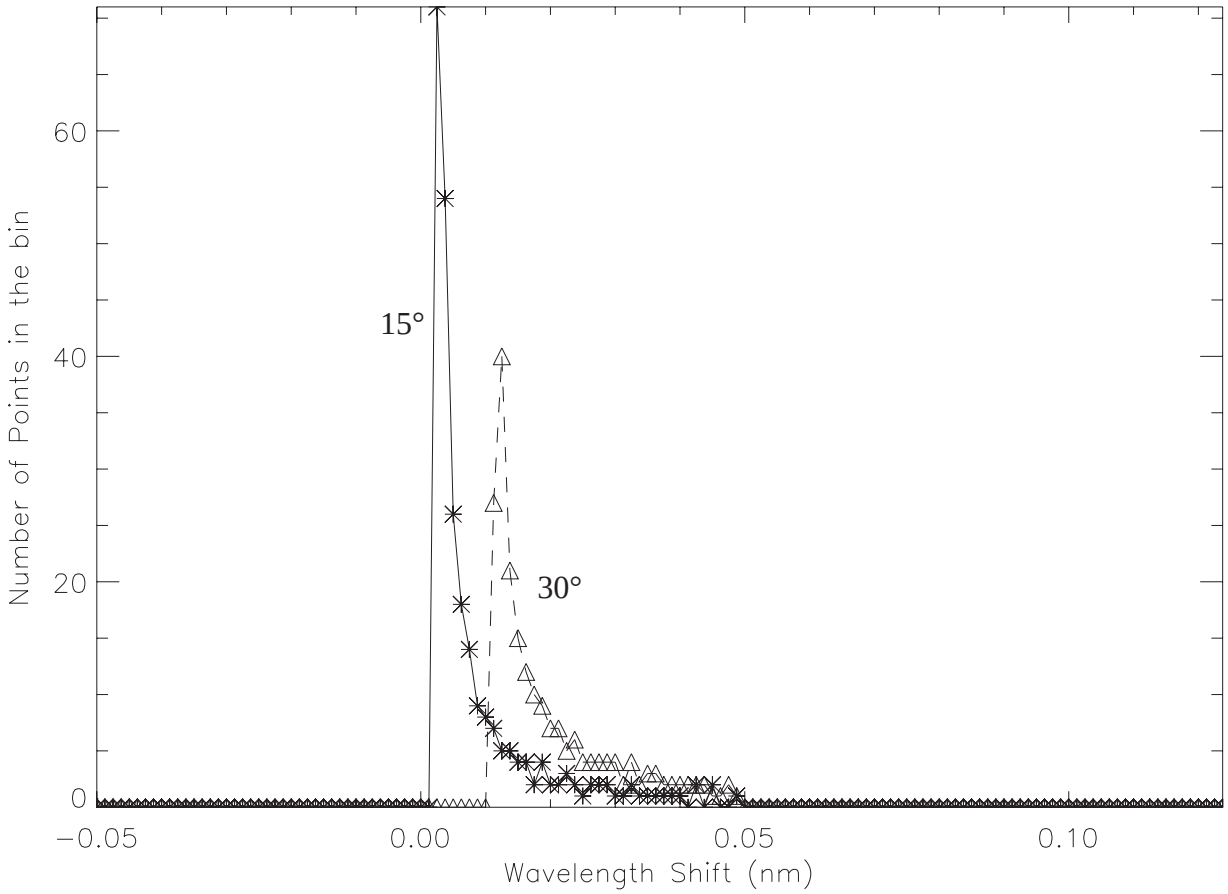

Figure 8.5: Lineshape obtained by an IDS system for a fluid with a linear flow profile, for chord angles 15° and 30°.

Since each chord is a different length, the variation in point number means that the magnitudes of the histograms for different chords cannot be compared. Nonetheless, Figures 8.5 and 8.6 give a good indication of the widths of the lines resulting from chords at the four angles.

8.2 Quadratic Flow Profile

A more realistic flow profile is a quadratic. This has the benefit of going to zero at some point away from the origin, allowing us to propose

$$| \mathbf{v} | = (260/R_0^2)(R_0 r - r^2)\text{km/s} \tag{8.5}$$

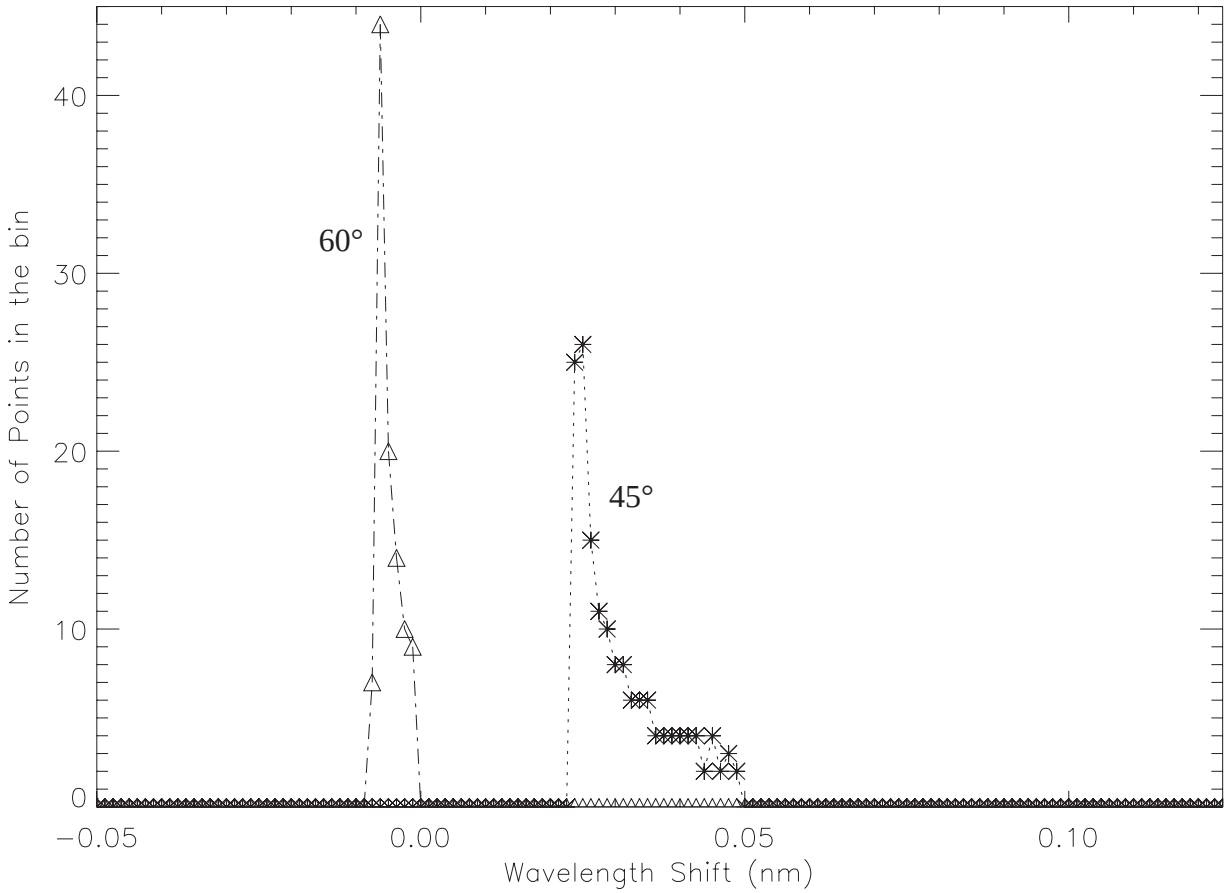

Figure 8.6: Lineshape obtained by an IDS system for a fluid with a linear flow profile, for chord angles 45° and 60°.

This is a quadratic with zeroes at the origin and at R_0, and with a central maximum of 65 km/s at $R_0/2$. THis is a more realistic flow profile because it makes sense that a differentially rotating fluid would have zero velocity parallel to its container walls due to friction and other dissipative forces.

The signal from each element of the chord is plotted in Figure 8.7. Unlike the linear profile, there is significant variation for different chord angles. The chord angle will affect how much of the high velocity part of the profile the chord "sees". For small angles, the chord will cut through the maxima, resulting in a lower-velocity signal in the middle. For other angles, however, the chord clearly passes through a region of high velocity. Again, we can represent the information in Figure 8.7 as a histogram (Figures 8.8 and 8.9) to get the lineshapes. The quadratic flow lineshapes do show evidence of double peaks for certain angles, probably due to the IDS seeing through the fluid to the oppositely directed maximum on the other side.

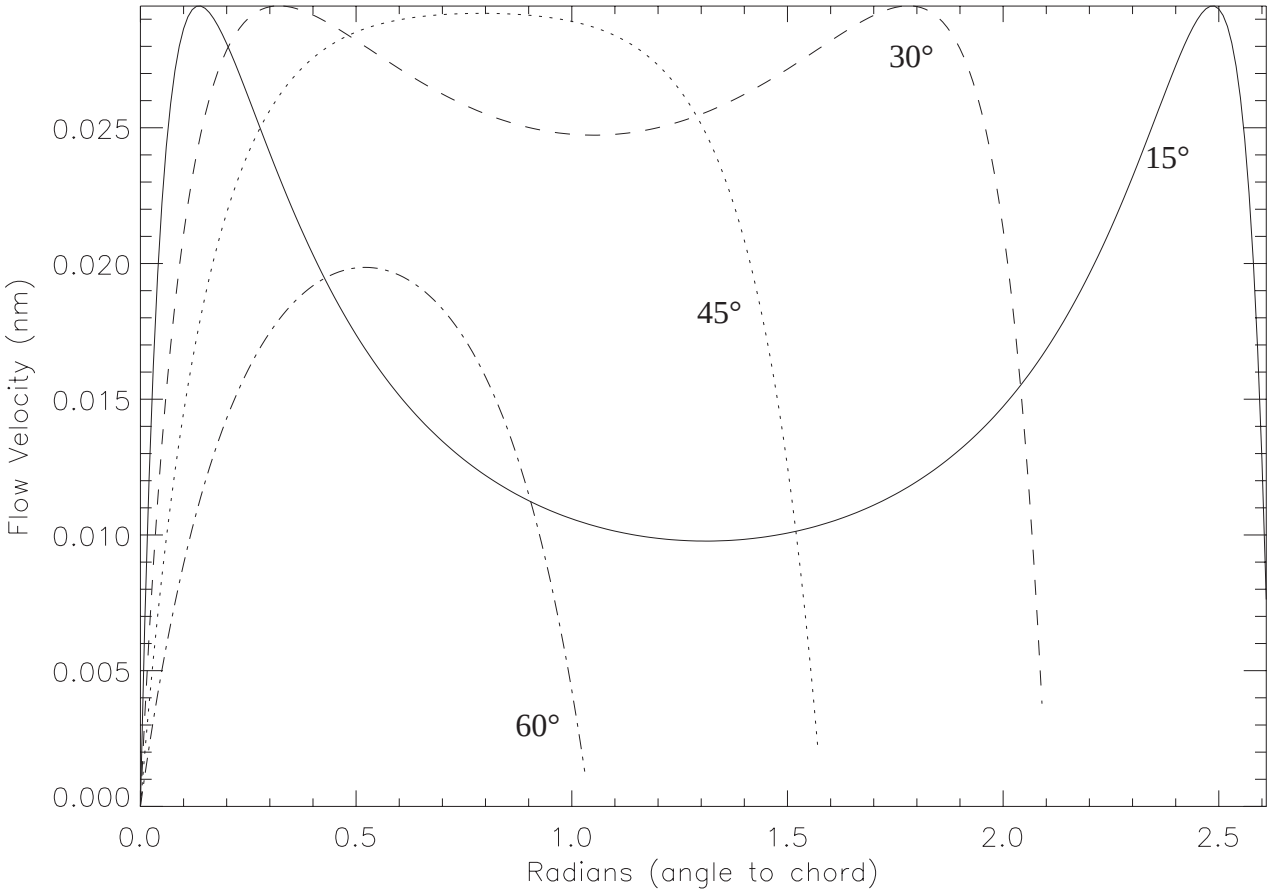

Figure 8.7: Signal from each chord element for four different chord angles through a fluid with a quadratic flow profile.

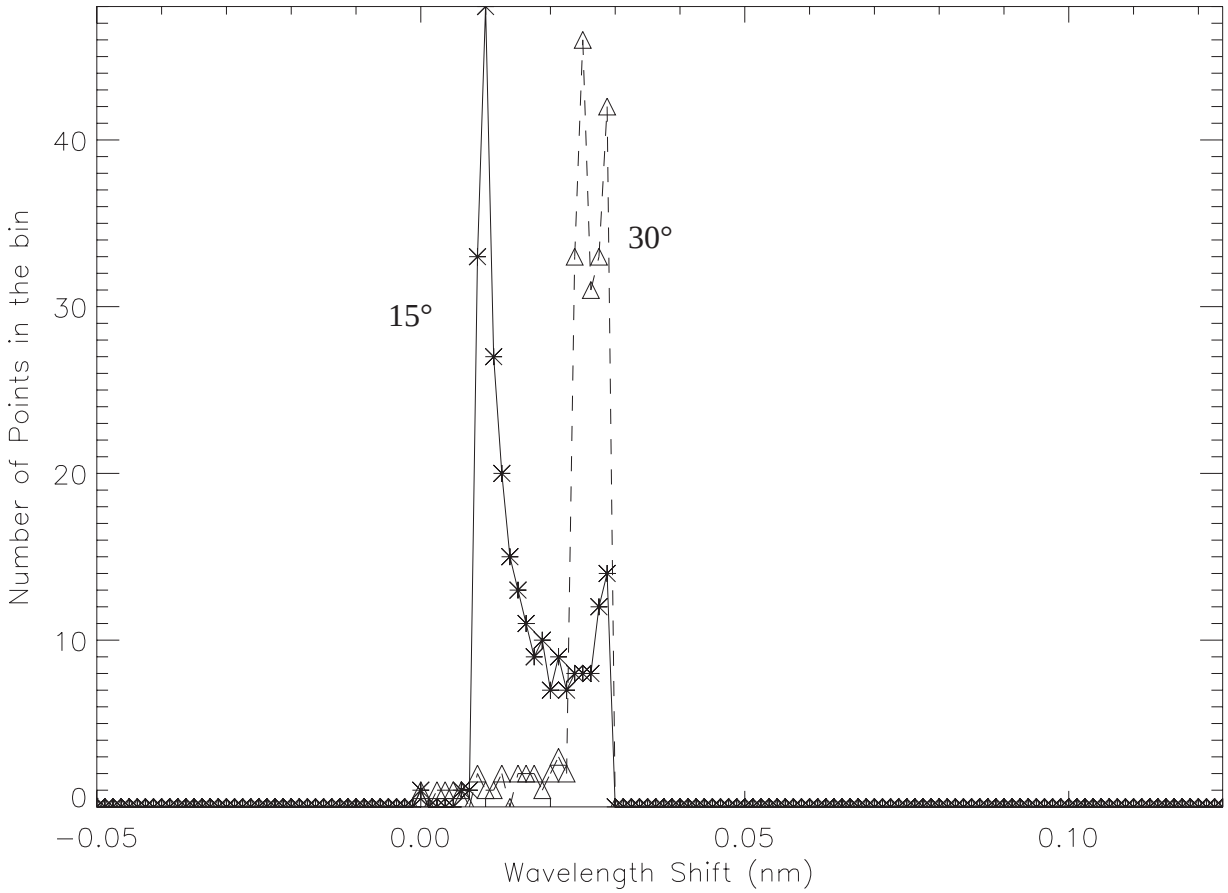

Figure 8.8: Lineshape obtained by an IDS system for a fluid with a quadratic flow profile, for chord angles 15° and 30°.

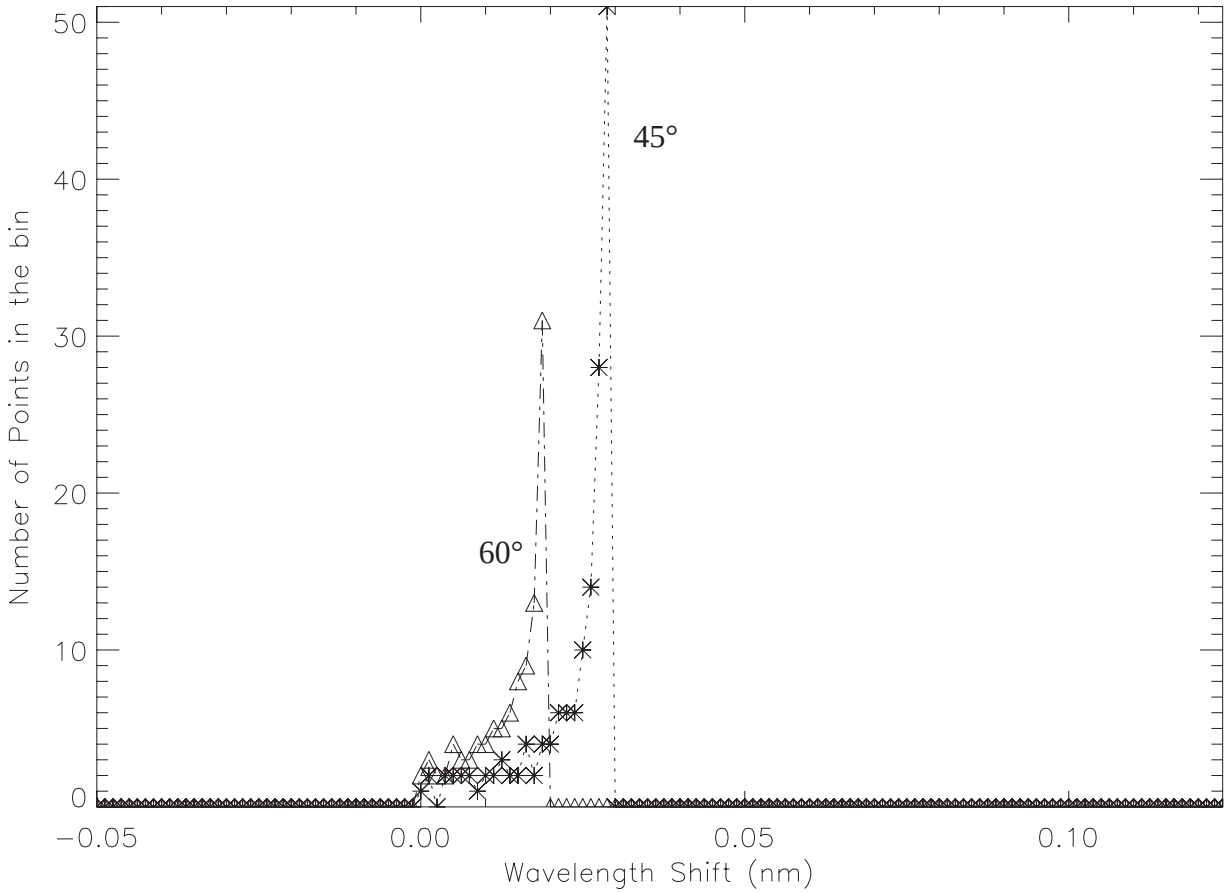

Figure 8.9: Lineshape obtained by an IDS system for a fluid with a quadratic flow profile, for chord angles 45° and 60°.

8.3 Cubic Flow Profile

The most simple profile that will get flows that point in opposite directions at different points along the same radial vector is a cubic. To better represent an FRC geometry, the zeros of the cubic are constrained. There should be a zero at the origin and at the outer wall, radius R. The third zero should be at $R/\sqrt{2}$, as discussed in Section 4.3. The peak flow velocity should be 65 km/h. All these dictate a flow profile like that of Equation 8.6 and Figure 8.10. Since the shear profile is a cubic with its central zero offset from the average of the other two zeros, the peaks are not of equal height. The positive peak has been arbitrarily chosen to be the one scaled to 65 km/s. The signal from each point on the chord for four chord angles is given by Figure 8.11. Turning the data in Figure 8.11 into a histogram (Figures 8.12 and 8.13) will separate the IDS signal into wavelength shift bins and show the lineshape.

$$\mid \mathbf{v} \mid \propto \frac{65}{0.0861581R^3}(r^3 - \frac{R}{2-\sqrt{2}}r^2 + (\frac{R^2}{2-\sqrt{2}} - R^2)r) \tag{8.6}$$

The location of the line centroids, the average of the histograms, is difficult to determine from the histogram plots. Averaging the $\mathbf{v} \cdot d\mathbf{s}$ IDS signal along the chord for all chord angles will determine it precisely, however (Figure 8.14).

This model has the problem that the cubic cannot give extrema of equal magnitude with a shifted central zero, but it does adequately illustrate the broadening of the lines due to velocity shear. In particular, the long shoulders on extreme-angle chords that become double-peaked distributions on middle-angle chords should be characteristic of a system with sheared flows (Figures 8.12, 8.13). Clearly the default, as seen for the 45° chord, is of a distribution much like the merged Gaussians of Figure 8.1, where the two shifts due to the opposite extrema are equally represented. As the chord angle deviates from this, one of the two flows should factor less and less into the signal and the lineshape should look like the 15° line in Figure 8.12, where only one peak figures prominently in the line, but with an extended shoulder that will pull the centroid away from the peak.

In any case, this simple model demonstrates how velocity shear does have the effect of artificially broadening emission lines by merging red- and blue-shifted lines into one, much wider, distribution. We expect such velocity shear to be present during FRC formation (Figure 4.4) and so this model does confirm that the very high "temperature" reported by the IDS system during the FRC formation period is a result of velocity shear.

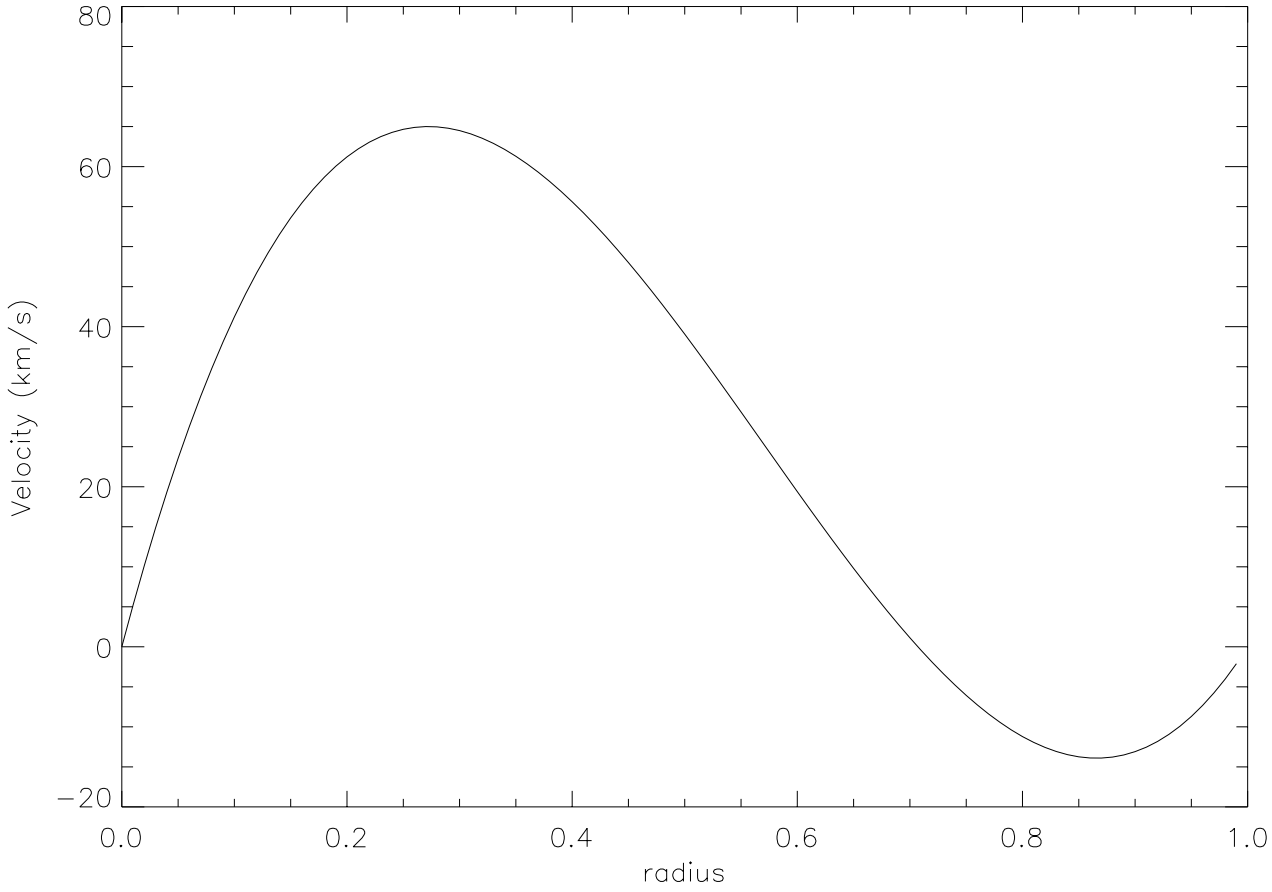

Figure 8.10: Velocity profile for the shear flow model. Note that the cubic forces one extremum to be larger than the other since the central zero is not at $R_0/2$.

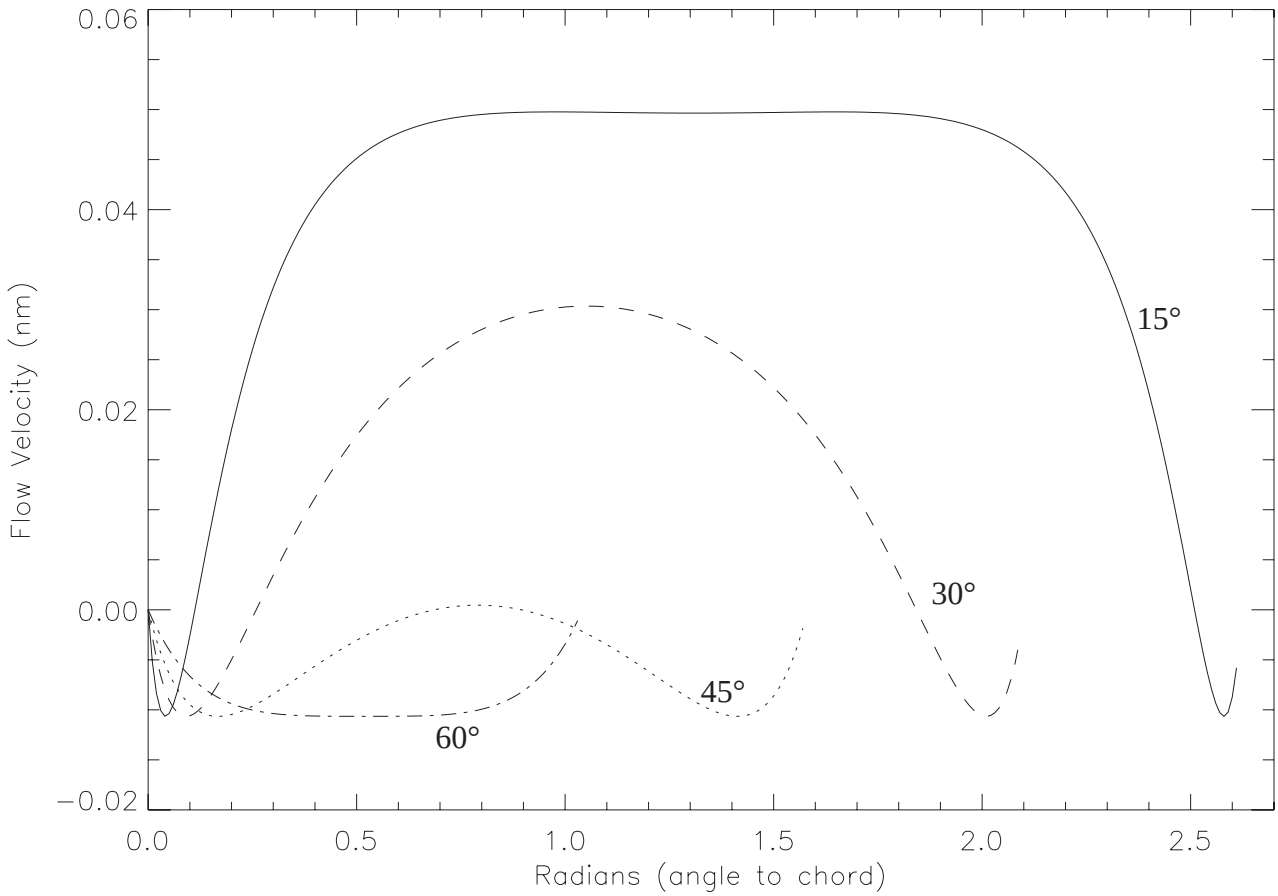

Figure 8.11: Signal obtained by an IDS system from each chord element for four different chord angles ϕ from a fluid with a cubic flow profile.

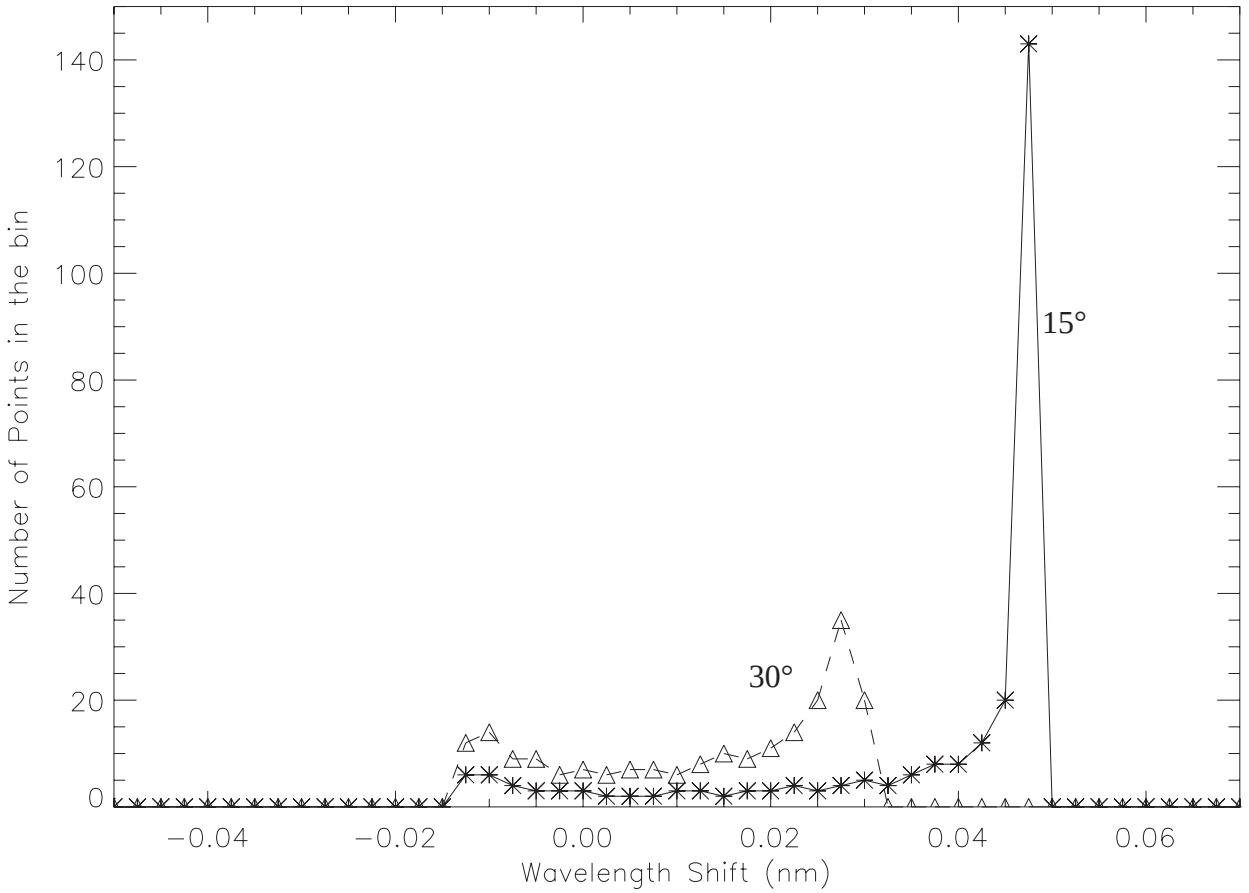

Figure 8.12: Lineshape obtained by an IDS system for a fluid with a cubic flow profile, for chord angles 15° and 30°.

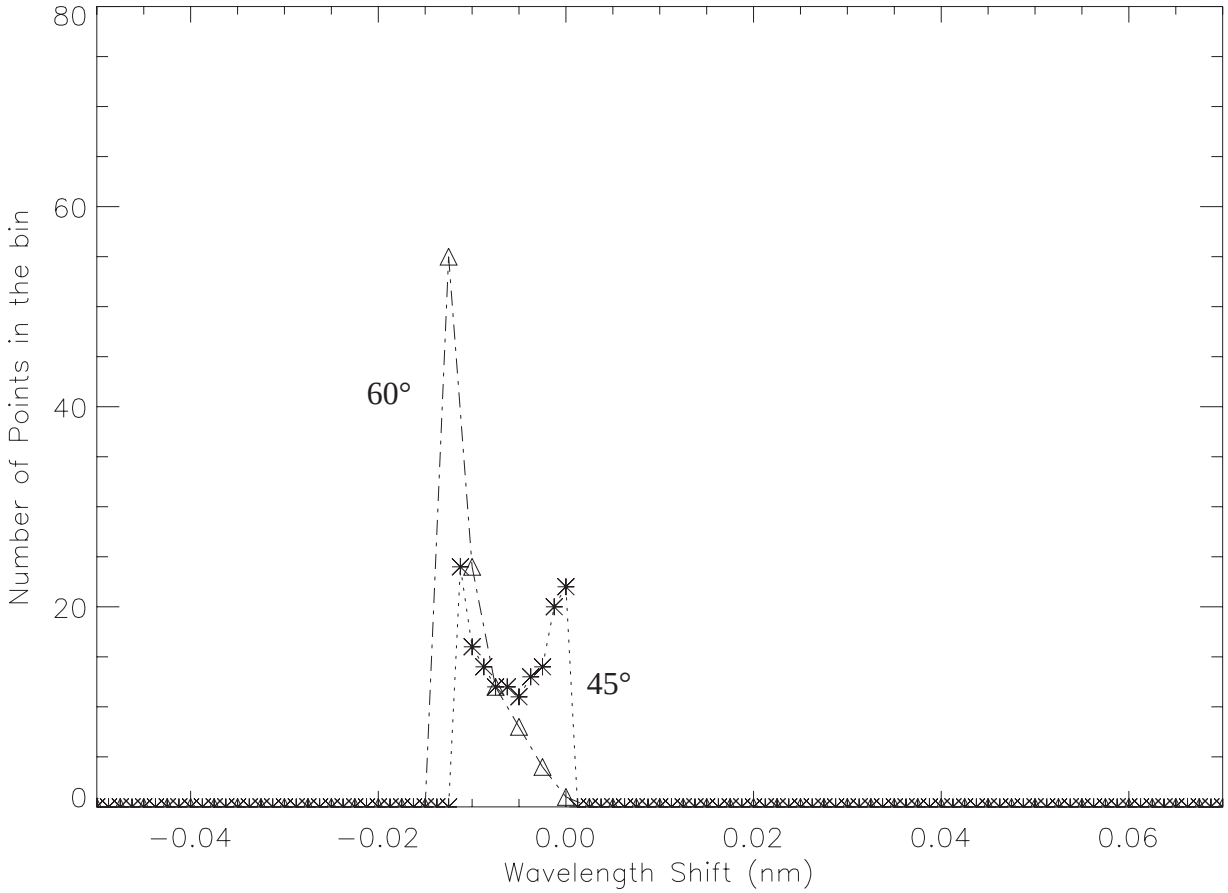

Figure 8.13: Lineshape obtained by an IDS system for a fluid with a cubic flow profile, for chord angles 45° and 60°.

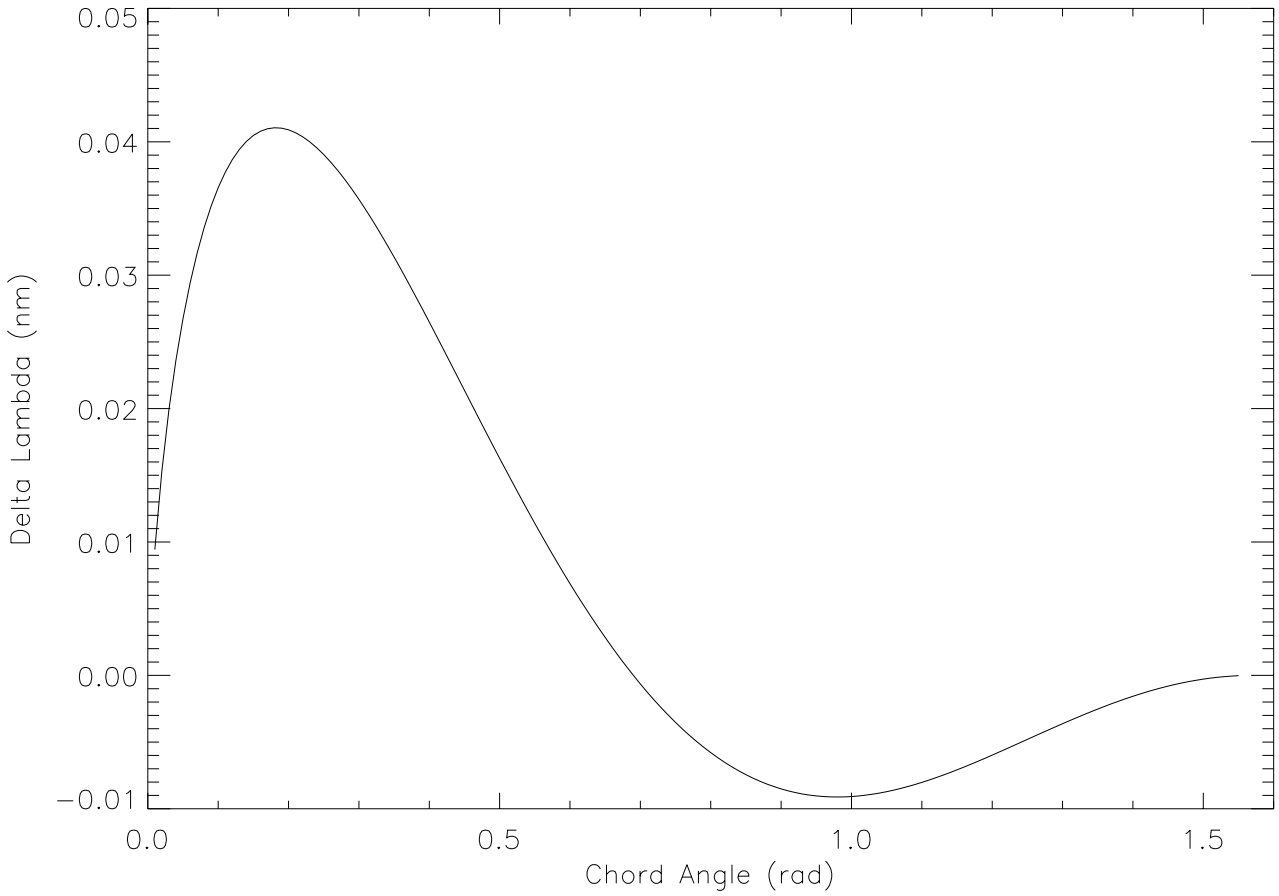

Figure 8.14: Centroid location for chord angle ϕ.

9 Conclusions

Currently, SSX's IDS system does not have the resolution needed to measure temperatures below approximately 200 eV. Since we expect the ion temperature to be approximately 20eV, the diagnostic cannot yet be used to detail the variation of temperature with time. The low resolution also affects the system's ability to determine the plasma's velocity since a precise measurement of the line is needed to determine its centroid. For these reasons, this thesis has not presented any new information about the temperatures and flow velocity within SSX-FRC.

Nevertheless, this thesis has shown promising signs that the only current impediment to precise, accurate, time-resolved temperature and velocity measurements is the system's resolution. The sudden drop in linewidth seen in Figure 7.8 is fully explained by the basic physics of the system, and an estimate of the line's width assuming velocity shear leads to velocity estimates that are consistent with previous measurements. Moreover, the exposition of these physics has exposed what I consider to be a problem with the seminal paper by Ono et al. [28], that the measured velocity shear was not taken into account when determining the ion temperature and hence had to go to some lengths to explain their very high measurements.

10 Acknowledgements

In conclusion, I hold the following people responsible for this thesis: my advisor, Michael Brown, without whom I never would have been introduced to the wonderful world of plasmas; Chris Cothran, for his invaluable help and advice; Carl Grossman, for dealing with the first draft of this thesis; and Jim Haldeman, for technical assistance.

11 Appendix: IDL Visualization Codes

The following is the IDL code used to generate the traces (Figure 7.2), lineshapes (Figure 7.6), velocity plot (Figure 7.7) and temperature plot (Figure 7.8). Comments are in parentheses, in boldface roman script.

```
pro showmapmt
```

(read data files into IDL and correct for crosstalk and anode non-uniformity)

```
data=read_ascii(data_start=1)
dy=150.0
time=reform(data.field1[0,*])*1.E6
ch11=reform(data.field1[1,*])*(1./0.977)
ch12=reform(data.field1[2,*])*(1./0.931)
ch13=reform(data.field1[3,*])*(1./0.951)
ch14=reform(data.field1[4,*])*(1./0.901)
data=read_ascii(data_start=1)
time=reform(data.field1[0,*])*1.E6
ch21=reform(data.field1[1,*])*(1./0.938)
ch22=reform(data.field1[2,*])*(1./0.933)
ch23=reform(data.field1[3,*])*(1./0.957)
ch24=reform(data.field1[4,*])*(1./0.921)
```

(plot the unaveraged corrected traces)

```
window,0
plot,[0],[0], background=1, color=0, /NODATA, xrange=[-10.0,140.0], $
xstyle=1, ystyle=1, yrange=[-4.25*dy,4.25*dy], xtitle="Time (us)"
oplot,time,ch11*1.E3-3.*dy,color=0
oplot,time,ch12*1.E3-2.*dy,color=0
oplot,time,ch13*1.E3-1.*dy,color=0
oplot,time,ch14*1.E3-0.*dy,color=0
oplot,time,ch21*1.E3+1.*dy,color=0
oplot,time,ch22*1.E3+2.*dy,color=0
oplot,time,ch23*1.E3+3.*dy,color=0
oplot,time,ch24*1.E3+4.*dy,color=0
```

(average every 100 points of data)

```
n=floor(n_elements(ch11)/100+1)
```

```
vsm=fltarr(n)
timesm=fltarr(n)
chsm=fltarr(8,n)
j=0
for i=0,n_elements(v)-1 do begin
timesm[j]=timesm[j]+time[i]*0.01
chsm[0,j]=chsm[0,j]+ch11[i]*0.01
chsm[1,j]=chsm[1,j]+ch12[i]*0.01
chsm[2,j]=chsm[2,j]+ch13[i]*0.01
chsm[3,j]=chsm[3,j]+ch14[i]*0.01
chsm[4,j]=chsm[4,j]+ch21[i]*0.01
chsm[5,j]=chsm[5,j]+ch22[i]*0.01
chsm[6,j]=chsm[6,j]+ch23[i]*0.01
chsm[7,j]=chsm[7,j]+ch24[i]*0.01
vsm[j]=vsm[j]+v[i]*0.01
if i mod 100 eq 0 then begin
j=j+1
endif
endfor
```

(this finds the centroid by line-averaging the signal, and finds the velocity from the doppler shift $\triangle\lambda \times c/\lambda_0 = v$)

```
vsmsm=fltarr(n)
totsm=fltarr(n)
for i=0,7 do begin
vsmsm=vsmsm+(float(i)-3.5)*reform(chsm[i,*])*0.032/229.7*3.E5
totsm=totsm+reform(chsm[i,*])
endfor
vsmsm=vsmsm/totsm
```

(take the velocity in later times as zero, so deduct from the whole)

```
vsmsm=vsmsm-mean(vsmsm[140:150])
```

(plot the centroid's velocity and uncertainty)

```
window,1
plot,[0],[0],background=1,/NODATA,xrange=[-10,140],xstyle=1,ystyle=1,$
yrange=[-60,15],ytitle="Flow velocity (km/s)",xtitle="Time (us)"
q=where(timesm gt 25)
oplot, timesm[q], vsmsm[q]-10., color=0,linestyle=1
```

```
oplot, timesm[q], vsmsm[q]+10., color=0,linestyle=1
oplot, timesm[q], vsmsm[q], color=0
```

(plot the lineshapes)

```
window,2
plot,[0],[0],background=1,color=0, /NODATA,xrange=[4.0,4.0], $
xstyle=1,ystyle=1,yrange=[10,150],xtitle="Position on Array (mm)"
xcoord=findgen(8)-3.5
oplot, xcoord, -1.E3*reform(chsm[*,60]), psym=-4, color=0,linestyle=1
oplot, xcoord, -1.E3*reform(chsm[*,80]), psym=-4,color=0,linestyle=2
oplot, xcoord, -1.E3*reform(chsm[*,100]), psym=-4,color=0,linestyle=3
oplot, xcoord, -1.E3*reform(chsm[*,120]), psym=-4,color=0,linestyle=4
oplot, xcoord, -1.E3*reform(chsm[*,140]) ,psym=-4,color=0,linestyle=0
```

(find the linewidth and hence the temperature (assuming a Gaussian lineshape) by turning the lineshapes into histograms and then taking the standard deviation of the histogram data)

```
p=findgen(8)-3.5
width=fltarr(200)
z=fltarr(8)
for k=0,199 do begin
z=-1.E3*reform(chsm[*,k])
hist=fltarr(1)
```

(set up the array for the histogram data–remember to get rid of this zero eventually)

```
for j=0,7 do begin
n=abs(floor(z[j]*100.))+1
```

(set the number of data points in the histogram bin by looking at the magnitude of the point; +1 since some points are zero and the array needs >0 elements)

```
x=fltarr(n)
x=x+p[j]
```

(fill the histogram bin with as many location coordinates as the point's magnitude)

```
if (n gt 1) then x=x[0:n-2]
```

(get rid of the extra element if the entry doesn't need it)

```
hist=[hist,x]
```

(add the histogram points just found into the histogram array)

```
     endfor
n=n_elements(hist)
hist=hist[1:n-1]
```

(get rid of the initial zero in the histogram data array)

```
&width[k]=stddev(hist)
endfor
```

(find the temperature from the standard deviation, assuming a Gaussian profile)

```
t=(findgen(200))
width=width*2.36*0.032
temp=((width/229.7)^2)*(12)*(7.16E-7)^(-2)
tempev=temp/11600.
```

(plot the temperature values)

```
window,8
plot, t, tempev, ytitle="Temperature (eV)", xtitle="Time (us)", $
xstyle=, xrange=[30,200], ystyle=1, background=1, color=0
end
```

12 Bibliography and References

References

[1] Auerbach, D. Ion Temperature Measurements in SSPX. Undergraduate Thesis, Swarthmore College 2001.

[2] Balandin, A.L., Ono, Y. Tomographic determination of plasma velocity with the use of ion Doppler spectroscopy. *European Physical Journal D*, **17**, 337. 2001

[3] Biskamp, D. *Magnetic Reconnection in Plasmas.* Cambridge University Press, Cambridge 2000.

[4] Bellan, P. *Spheromaks.* Imperial College Press, London 2000.

[5] Bellan, P., Yee, J., Hansen, J.F. Spheromaks, Solar Prominences, and Alfven instability of current sheets. *Earth Planets Space*, **53**, 495. 2001

[6] Carolan, P.G., O'Connel, R. A multichord spectrometer using an 8×8 anode photomultiplier *Rev. Sci. Inst.*, **66**, 1184. 1995

[7] Cothran, C.D., Falk, A., Fefferman, A., Landreman, M., Brown, M.R., Schaffer, M.J. Spheromak merging and field reversed configuration formation at the Swarthmore Spheromak Experiment. *Phys. Plasmas*, **10**, 1748 2003

[8] Den Hartog, D.J., Fonck, R.J. A fast spectroscopic diagnostic for the measurement of plasma impurity ion dynamics. *Rev. Sci. Inst.*, **65**, 3238. 1994

[9] Den Hartog, D.J., Holly, D.J. A simple, low-cost, versatile charge-coupled device spectrometer for plasma spectroscopy. *Rev. Sci. Inst.*, **68**, 1036. 1997

[10] Dorland, W. Single Particle Motion. National Undergraduate Fellowship Presentation 2004.

[11] Engstrom, R.W. *Photomultiplier Handbook.* RCA, Lancaster, PA 1980.

[12] Falk, A. Dynamics of Field-Reversed-Configuration in SSX. Undergraduate Thesis, Swarthmore College 2003.

[13] Fefferman, A. Formation and Stability of Spheromak/Field Reversed Configuration (FRC) Hybrids in SSX-FRC Undergraduate Thesis, Swarthmore College 2003.

[14] Freidberg, J. P. *Ideal Magnetohydrodynamics.* Plenum Press, London 1987

[15] Fiksel, G., Den Hartog, D.J., Fontana, P.W. An optical probe for local measurements of fast plasma ion dynamics. *Rev. Sci. Inst.*, **69**, 2024. 1988

[16] Goldston, R.J., Rutherford, P.H. *Introduction to Plasma Physics.* Institute of Physics Publishing, Philadelphia 1995.

[17] Hanasz, M., Lesch, H. Conditions for fast magnetic reconnection in astrophysical plasmas. *Astronomy and Astrophysics*, **404**, 389. 2003

[18] Hegna, C. Magnetohydrodynamics. National Undergraduate Fellowship Presentation 2004.

[19] Heinrich, F., Stoll, H.-P., Hoffmann, P., Scheer, H.-C. Ion beam diagnostics by Doppler shifted light emissions . *Rev. Sci. Inst.*, **63**, 3063. 1992

[20] Hutchinson, I.H. *Principle of Plasma Diagnostics.* Cambridge University Press, Cambridge 2002.

[21] Hutley, M.C. *Diffraction Gratings.* Academic Press, London 1982.

[22] Hsu, S.C., Carter, T.A., Fiksel, G., Ji, H., Kulsrud, R.M., Yamada, M. Experimental study of ion heating and acceleration during magnetic reconnection. *Phys. Plasmas*, **8**, 1916. 2001

[23] Kornack, T.W., Sollins, P.K., Brown, M.R. Experimental observation of correlated magnetic reconnection and Alfvénic ion jets. *Phys. Rev. E*, **58**, 1063. 1998

[24] Kornack, T.W. Magnetic Reconnection Studies on SSX. Undergraduate Thesis, Swarthmore College 1998.

[25] Kulsrud, R.M. Magnetic Reconnection: Sweet-Parker versus Petschek. *Earth Planets Space*, **53**, 417. 2001

[26] Landreman, M. The Three-Dimensional Structure of Magnetic Reconnection in SSX. Undergraduate Thesis, Swarthmore College 2003.

[27] Loewen, E.G., Popov, E. *Diffraction Gratings and Applications.* Marcel Dekker, New York 1997.

[28] Ono, Y., Yamada, M., Akao, T., Tajima, T., Matsumoto, R. Ion Acceleration and Direct Ion Heating in Three-Component Magnetic Reconnection. *Phys. Rev. Letters*, **76**, 3328 1996

[29] Ono, Y., Inomoto, M., Okazaki, T., Ueda, Y. Experimental investigation of three-component magnetic reconnection by use of merging spheromaks and tokamaks. *Phys. Plasmas*, **4**, 1953 1997

[30] Ono, Y., Matsuyama, T., Umeda, K., Kawamori, E. Spontaneous and artificial generation of sheared-flow in oblate FRCs in TS-3 and 4 FRC Experiments. *Nucl. Fusion*, **43**, 649. 2003

[31] Pedrotti, F., Pedrotti, L. *Introduction to Optics.* Prentice Hall, Upper Saddle River, NJ 1993.

[32] Svanberg, S. *Optical and Molecular Spectroscopy.* Springer-Verlag, Berlin 1992.

[33] Tuszewski, M.G. Field-Reversed Configurations Without Toroidal Field. *Nucl. Fusion*, **28**, 2033. 1988

[34] Ueda, Y., Ono, Y. High-power heating of spherical tori by use of magnetic reconnection. *Earth Planets Space*, **53**, 527. 2001

[35] Yamada, M., Ono, Y., Hayakawa, A., Katsurai, M., Perkins, F.W. Magnetic Reconnection of Plasma Toroids with Cohelicity and Counterhelicity. *Phys. Rev. Letters*, **65**, 721. 1990